Alejandro Alonzo-Garcia[1]
CONACYT-CIDESI Sede-CAMPECHE,
Carretera Champotón-Cd del Carmen 408,
Ciudad del Carmen,
Campeche C. P. 24150, Mexico
e-mail: aalonzo@conacyt.mx

Ana T. Mendoza-Rosas
CONACYT-CIDESI Sede-CAMPECHE,
Carretera Champotón-Cd del Carmen 408,
Ciudad del Carmen,
Campeche C. P. 24150, Mexico
e-mail: atmendoza@conacyt.mx

Martín A. Díaz-Viera
Gerencia de Ingeniería de Recuperación Adicional,
Instituto Mexicano del Petróleo,
Eje Central Lázaro Cárdenas 152,
Ciudad de México C. P. 07730, Mexico
e-amil: mdiazv@imp.mx

Sergio A. Martínez-Delgadillo
Depto Ciencias Básicas,
Universidad Autónoma Metropolitana,
Av. San Pablo 180, Azcapotzalco,
Ciudad de México C. P. 07740, Mexico
e-mail: samdmas@gmail.com

Edgar G. Martínez-Mendoza
Posgrado en Ciencias de la Tierra,
Universidad Nacional Autónoma de México,
Ciudad de México C. P. 24150, Mexico
e-mail: edgarg.martinezm@gmail.com

Assessment of Low-Re Turbulence Models and Analysis of Turbulent Flow in Porous Media Consisting of Square Cylinders With Different Diameter Ratios

This paper presents a comparative study of volume average predictions between low-Reynolds-number (LRN) turbulence models: Abe–Kondoh–Nagano (AKN), Lam–Bremhorst, Yang–Shih, standard k–ϵ, and k–ω. A porous medium, which represents conditions in which the flow path changes rapidly, was defined as an infinite array of square cylinders. In addition, to explore the effect of particle size on the rapid expansion and contraction of the flow paths, the diameter ratio (DR) of the square cylinders was systematically varied from 0.2 to 0.8. This generalization revealed new insights into the flow. The Reynolds number (Re_D) covered a turbulent range of 500 to 500×10^3, and the porosity ϕ was varied from 0.27 to 0.8. The correlations of the turbulent kinetic energy (k), its dissipation rate (ε), and macroscopic pressure gradient as a function of ϕ, which are useful in macroscopic turbulence modeling, are presented. The results show that the AKN model yields better predictions of the volume-averaged flow parameters because it is better suited to reproduce recirculation zones. For all the DRs, at high ϕ, the distances between walls are high, and the interstitial velocities are low. Consequently, wake flows are produced, and energy losses by friction are moderate. As the flow becomes increasingly bound, the wakes are suppressed and disrupted, and k and ε increase owing to shear layer interactions and frictional forces. Distinctive low-velocity recirculation patterns appear inside pores depending on DR. [DOI: 10.1115/1.4048284]

Introduction

As turbulence generally enhances heat transfer, mixing, chemical reactions, and energy dissipation at the smallest scales, it is essential to understand its effects in porous media to support engineering phenomena and applications, for example, flow in fracture models, enhanced oil recovery techniques, irrigation systems, and the design of catalytic reactors, fluidized beds, and static mixers. To determine the pressure drop in porous percolation networks and its relationships with turbulent parameters within porous systems, tailored analytical, experimental, and numerical tools are required.

Velocity measurement techniques such as hot-wire anemometry are difficult to implement in porous media, as the solid walls of the matrix may interfere with the probe. Other techniques such as laser Doppler velocimetry or particle image velocimetry, require translucent walls and fluids [1,2]. Matching the refraction index of the pore walls to that of the fluid is not a trivial task, in part because manufacturing a porous matrix with translucent walls involves additional complexities. For this reason, computational fluid dynamics has emerged as a useful alternative for understanding turbulent flow in a porous medium.

Wood et al. [3] recently presented a comprehensive review of the most important methodologies, advances, and challenges of modeling turbulent flow in porous media. Different formulations of the Reynolds number have been established. For example, the pore Reynolds number Re_p is defined in terms of the volume-averaged intrinsic velocity $\langle u \rangle^f$, whereas Re_D is the same dimensionless number, but is defined in terms of the Darcy velocity u_D. Other definitions use the representative volume element (RVE) height (H) instead of the particle diameter (D). The appropriate parameters must be selected for each model, and according to Wood et al. [3], there is no formulation that can be considered universally optimal.

The most powerful numerical approach to modeling turbulent flow is direct numerical simulation (DNS). This technique can handle turbulent motions at all the relevant temporal and spatial scales without any modeling assumptions [3,4]. However, because the smallest dissipative scales (the Kolmogorov scales) demand high spatial and temporal resolution, DNS studies rely on the use of powerful supercomputers and have focused mostly on the lower range of the turbulent regime (i.e., $Re_p < 5000$). For example, Jin et al. [5] studied turbulence in porous media consisting of an infinite array of square cylinders using grids of up to 384×10^6 cells for $500 < Re_p < 1000$. Another representative work is that of Chu et al. [6], where grids with as many as 200×10^6 cells were used to simulate similar porous media at $500 < Re_p < 1500$.

Large eddy simulation (LES) is also a powerful approach and has less stringent resolution requirements. Based on the energy cascade model of Kolmogorov, LES resolves the largest eddies directly, considering that they contain most of the flow kinetic energy, whereas the dissipative eddies are accounted for by a subgrid-scale model assuming isotropic or anisotropic conditions [7]. Using the LES technique, Suga and coworkers have studied turbulent flow in different types of porous media at $Re_p < 3500$ using grids ranging from 4.2×10^6 to 21×10^6 cells [8,9]. Important parameters such as the pressure strain terms, heat fluxes,

[1]Corresponding author.

Contributed by the Fluids Engineering Division of ASME for publication in the Journal of Fluids Engineering. Manuscript received October 23, 2019; final manuscript received August 15, 2020; published online October 12, 2020. Assoc. Editor: Haoxiang Luo.

Reynolds stresses, and other turbulent quantities were discussed. Although LES is less computationally demanding than DNS, its implementation requires well-refined grids and a large number of time steps to deliver statistically converged solutions. The latter is inconvenient for studies that involve multiple simulations.

For this reason, Reynolds-averaged Navier–Stokes (RANS) turbulence models have been applied in parametric studies of porous media and have shown reasonable agreement with both DNS [10] and LES [11,12], but without the need for large computational resources. This approach is based on the ensemble averaging of the mean and fluctuating components of the Navier–Stokes flow variables. When this averaging procedure is used, the fluctuating velocity terms are used to obtain the Reynolds stress tensor, which is then modeled using an eddy viscosity formulation. Among those RANS-based turbulence models, the two-equation models of the k–ε or k–ω family have been implemented in a wide variety of engineering fields. These models assume isotropic turbulence and thus are commonly used to simulate high-Reynolds-number flows, where their predictions are considered valid, especially in regions far from the walls. Examples of successful applications include the design of airflow distribution systems, vehicle aerodynamics, nozzles and diffusers in turbomachinery, and cooling elements in electronic devices [13].

However, it is known that in the near-wall region, these models yield unsatisfactory results, because their formulations do not account for the rapid attenuation of the velocity fluctuations in zones close to the viscous sublayer [14]. For highly confined domains such as those in porous media, this drawback is particularly important. To address this shortcoming, the original models are corrected by applying damping functions to the production and destruction terms of the ε transport equation, as well as in the turbulent viscosity. The resulting modified versions are known as low-Reynolds-number (LRN) turbulence models.

Two approaches can be used to develop macroscopic turbulence models of porous media; both use RVEs to model periodic porous structures. In the first approach, the Reynolds averaging operator is applied to the volume-averaged macroscopic equations of the turbulent kinetic energy (k) and its dissipation rate (ε) [15,16]. This procedure accounts for the turbulence in the domain from a global perspective. In the second approach, the RANS equations are obtained and then integrated over an RVE to obtain the macroscopic turbulence model equations [17,18]. Because the second approach accounts for the turbulence within pores, it has been applied to various types of porous media [16,19]. The feasibility of simulating turbulence using this approach has been confirmed by Nakayama and Kuwahara [18] and Pedras and Lemos [20], and more recently by Yang et al. [16] and Kundu et al. [21]. These works reported the correlations among the macroscopic pressure gradient (MPG), k, and ε as functions of the porosity and particle geometry in homogeneous porous domains.

Different formulations of the damping functions of the LRN turbulence models have been presented in the literature; the most common are those of the Lam–Bremhorst (LB), Abe–Kondoh–Nagano (AKN), and Yang–Shih (YS) models. For example, the damping function applied to the eddy viscosity in the LB model employs the one-equation model proposed by Hassid and Pored [22], and it has been tested in a fully developed pipe flow [23]. The AKN model applies the Kolmogorov velocity scale in the damping formulas for both the eddy viscosity and the ε transport, and it has been validated for backward-facing step flows [24]. The YS model applies a characteristic time scale that approaches the Kolmogorov time scale in the near-wall region, and it has been validated in boundary layers with favorable, adverse, and zero pressure gradient [25].

These LRN models have been applied individually to porous media to study turbulence in homogeneous domains. For example, Kuwahara et al. [26] used the AKN model to simulate turbulent flow over square cylinders of infinite length. Kundu et al. [12] employed the YS model to simulate the flow over an arrangement of infinite circular cylinders, and Yang et al. [16] applied the standard $k-\varepsilon$ (STD) model with enhanced wall treatment to perform three-dimensional calculations of flow domains composed of arrangements of spheres, ellipses, and cubic elements.

According to our review of the state of the art, the only work that compared the LRN turbulence models in the same framework was that of Hrenya et al. [10], which focused on the fully developed turbulence inside a conduit. Those authors reported differences in the predicted velocity, turbulent viscosity, and k profiles, but they did not compare any volume-averaged quantities. Each LRN turbulence model has been developed under different assumptions, and despite the importance of the model accuracy, there is little information on the most accurate model of k and ε inside porous media, especially in separated flows. Moreover, other formulations, such as the LRN version of the k–ω model (LR k–ω) have not been explored. Consequently, a comparative study is highly desirable to generate workbench data for reliable simulations, especially when volume-averaged quantities are crucial.

It is well known that porous materials do not always consist of solid elements having the same geometry and length scale. Instead, they may consist of particles of different sizes (i.e., grain diameters) sorted in different ways. Examples include hierarchical porous carbons [27], foams [28], nanomaterials [29], and rock formations [30]. In these cases, the macroscopic behavior of the fluid flow through the porous medium is determined by the local mean velocities and turbulent parameters in the flow paths. Over the last decade, extensive efforts have been made to understand turbulent flows [12,19,21], and the correlations between k, ε, and the MPG have been proposed for porous media consisting of staggered arrays of particles of the same diameter. However, distinctive flow patterns are expected in domains composed of particles with different sizes because their flow paths rapidly expand or contract. To systematically replicate these conditions, the diameter ratio (DR) has been included in the analysis.

Some insight about the effect of the particle size variation could be found, for instance, in the work of Kuwata and Suga, who implemented LES to simulate three-dimensional fractal arrangements by applying the lattice Boltzmann method [8]. Important differences in quantities such as the permeability, the Forchheimer coefficient, and k were found between the body-centered cubic array and the fractal and staggered rectangular arrays.

Accordingly, this work considers the effect of the diameter ratio and porosity on the turbulent structures in an array of infinite cylinders with square cross sections. The porosity (ϕ) was varied from 0.27 to 0.8, and the diameter ratio, $DR = d/D$, ranged from 0.2 to 0.8 at intervals of 0.2. Here, the Reynolds number is defined as $\mathrm{Re}_D = u_D D/\nu$ and is based on the largest particle diameter D. The variables ν and u_D represent the kinematic viscosity and Darcy velocity, respectively. The latter is related to the intrinsic velocity as $u_D = \phi\langle u\rangle^f$. To cover a large portion of the turbulent regime, it was varied from 500 to 500×10^3. One of the goals of this work is to elucidate the effect of DR on the velocities, vorticity, and turbulence variables inside pores, and to present new correlations between k, ε, and the MPG. The latter could be helpful for understanding flow features and energetic losses in engineering applications such as static and moving fluidized beds, fabrics, nuclear power facilities, and oil well flows, among others.

In addition, this paper presents an updated assessment of the AKN, LB, YS, STD, and LR k–ω turbulence models, with a focus on flow over an infinite array of square cylinders. The assessment considers the ability of these models to predict volume-averaged values of key parameters. It is important because the LRN turbulence models have been tested by comparing profiles but not volume-averaged quantities in pipe flows or infinite flat plates without reattachment and separation. Therefore, it could support more confident selection of the most appropriate model for simulating more complex flows (multiphase flows, flow in fracture networks, and heat-transfer, among others).

This paper is structured as follows. The Computational Methods section describes the porous domains, microscopic governing

equations, damping terms, and applied boundary conditions (BCs). The macroscopic modeling assumptions are summarized, and the grid independence is analyzed. In the Results and Discussion section, the LRN turbulence models are assessed using the volume-averaged parameters as a function of Re_D and ϕ. The studied domain is a porous medium consisting of a spatially periodic array of square cylinders of the same diameter. In addition, the effects of the DR and the porosity are described in terms of the volume-averaged values and the main flow patterns are shown using dimensionless contour maps of u_D, ω, k, and ε.

Computational Methods

Porous Model Domain. The porous medium is modeled as an infinite array of large square cylinders in a symmetrical repetitive arrangement with smaller cylinders surrounding them in the domain. As shown in Fig. 1(*a*), the RVE height (H) is fixed, and the diameter ratio of the small and large cylinders (DR $= d/D$) is 0.2, 0.4, 0.6, and 0.8. The corresponding ϕ values of 0.72, 0.63, 0.48, and 0.27, respectively, were calculated using $\phi = 1 - (D^2 + 3d^2)/H^2$. The geometry of the RVEs is illustrated in Fig. 1(*b*). The representative lengths of the components of this RVE were chosen assuming a fully developed macroscopic flow directed parallel to the x coordinate. Because the domain is symmetrical along the normal direction and periodic in the streamwise direction, an RVE consisting of a large cylinder surrounded by smaller ones was selected. The size of the RVE was determined according to the works described in Refs. [18], [20], and [21]. The validity of this selection was tested by comparing the solutions for DR $= 0.6$, $\phi = 0.48$, and $Re_D = 50 \times 10^3$, and DR $= 0.6$, $\phi = 0.8$, and $Re_D = 5 \times 10^3$ obtained using domains that were four times larger.

At the inlet–outlet boundaries of the RVE, denoted as *ab-a'b'* in Fig. 1(*b*), a periodic BC was imposed, whereas on the upper and lower boundaries (*cd–c'd'*), the flow was considered to be symmetric. In the large cylinder and surrounding smaller ones, the nonslip BC was applied. As mentioned previously, the Reynolds number Re_D covered the turbulent regime from 500 to 500×10^3.

To better understand the relationship between porosity and flow characteristics, ϕ was varied from 0.27 to 0.8 by adjusting the H value of the RVEs for all the DR cases. As an example, Fig. 2 shows the variation in the RVE at DR $= 0.6$ and porosities of 0.3, 0.6, and 0.8. Because of the changes in H at a fixed DR, the smaller squares were closer to the large one for low values of ϕ. Conversely, for high ϕ, the smaller cylinders were more distant, i.e., $H1 < H2 < H3$.

Microscopic Governing Equations and Damping Terms. A steady incompressible Newtonian flow inside the pores was considered. The RANS equations of the mass and momentum are given by

$$\frac{\partial \overline{u}_i}{\partial x_i} = 0 \tag{1}$$

$$\rho_f \frac{\partial \overline{u}_j \overline{u}_i}{\partial x_j} = -\frac{\partial \overline{P}}{\partial x_i} + \frac{\partial}{\partial x_j}\left[\mu \frac{\partial \overline{u}_i}{\partial x_j} - \rho_f \overline{u_i' u_j'}\right] \tag{2}$$

The effect of the turbulent Reynolds stresses in the momentum equations was accounted for using the Boussinesq approximation according to

$$-\rho_f \overline{u_i' u_j'} = \mu_t \left(\frac{\partial \overline{u}_i}{\partial x_j} + \frac{\partial \overline{u}_j}{\partial x_i}\right) - \frac{2}{3} k \delta_{ij} \tag{3}$$

The turbulent viscosity was defined as

$$\mu_t = \rho_f f_\mu C_\mu \frac{k^2}{\varepsilon} \tag{4}$$

The k and ε transport equations are given by

$$\frac{\partial}{\partial x_i}(k\overline{u}_i) = \frac{\partial}{\partial x_j}\left[\left(\nu + \frac{\nu_t}{\sigma_k}\right)\frac{\partial k}{\partial x_j}\right] - \overline{u_i' u_j'}\frac{\partial \overline{u}_i}{\partial x_j} - \varepsilon \tag{5}$$

$$\frac{\partial}{\partial x_i}(\varepsilon\overline{u}_i) = \frac{\partial}{\partial x_j}\left[\left(\nu + \frac{\nu_t}{\sigma_\varepsilon}\right)\frac{\partial \varepsilon}{\partial x_j}\right] + f_1 C_{1\varepsilon}\frac{\varepsilon}{k}\left[\overline{u_i' u_j'}\frac{\partial \overline{u}_i}{\partial x_j}\right] - f_2 C_{2\varepsilon}\frac{\varepsilon^2}{k} \tag{6}$$

In Eq. (4), the damping terms f_μ of the LRN turbulence models are based on the formulations presented in Table 1. Additionally,

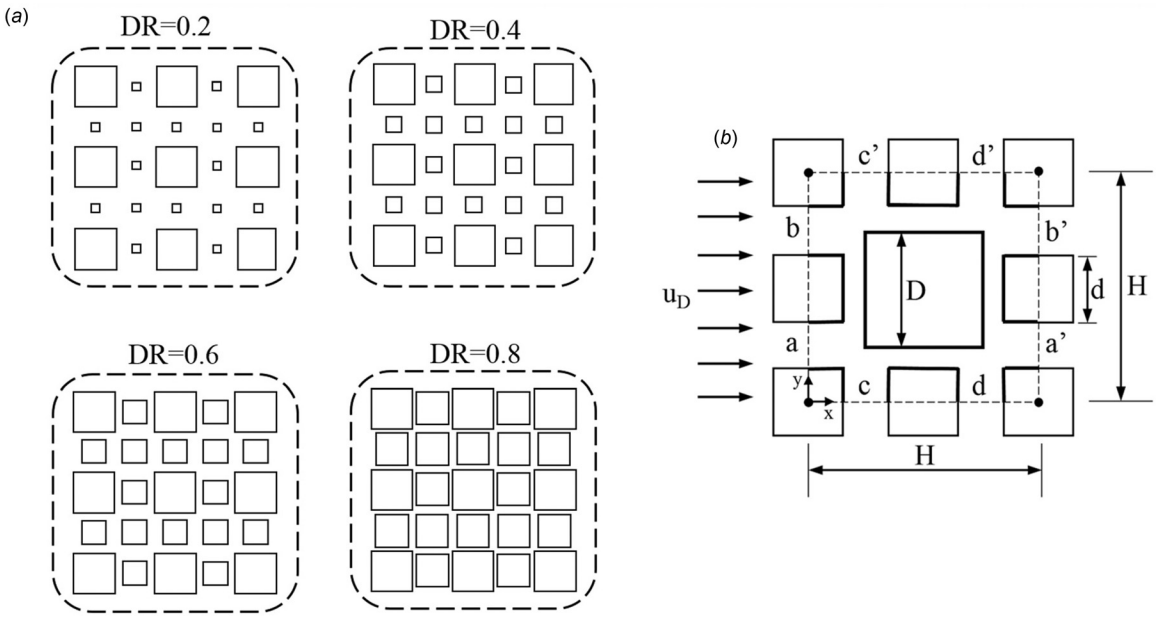

Fig. 1 Porous domains: (*a*) schematic representation as a function of the diameter ratio and (*b*) two-dimensional RVE geometrical description

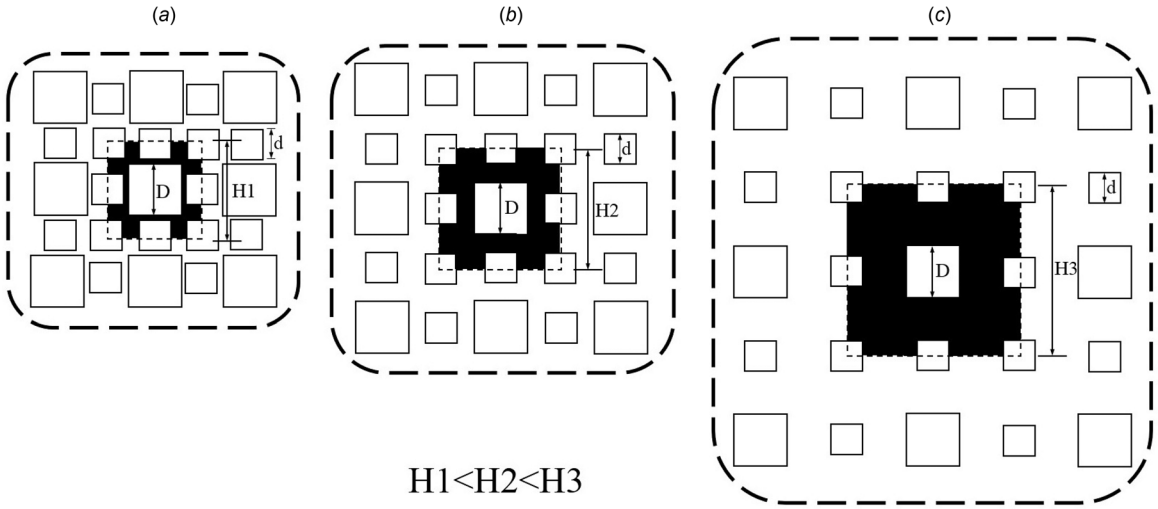

Fig. 2 Representative volume elements for DR = 0.6 and porosity values: (*a*) $\phi = 0.3$, (*b*) $\phi = 0.6$, and (*c*) $\phi = 0.8$

Table 1 Damping functions of the turbulent viscosity relations

Model	f_μ
AKN[a,d]	$[1-\exp(-y^*/14)]^2\{1+(5/R_t^{0.75})\exp[-(R_t/200)^2]\}$
LB[a,b]	$[1-\exp(-0.0165R_y)]^2(1+20.5/R_t)$
YS[b]	$[1-\exp(-1.5\times10^{-4}R_y-5.0\times10^{-7}R_y^3-1.0\times10^{-10}R_y^5)]^2$
LRk-ω[c]	$\dfrac{\alpha^*_\infty(\alpha^*_0+\mathrm{Re}_{t\omega}/R_k)}{\alpha^*}(1+\mathrm{Re}_{t\omega}/R_k)^{-1}$

[a] $R_t = k^2/\nu\varepsilon$.
[b] $R_y = y\sqrt{k}/\nu$.
[c] $R_{t\omega} = k/\nu\omega$.
[d] $y^* = u_K y/\nu$.

Table 2 lists the damping functions for the production and destruction of the ε terms. In the LRN turbulence model runs, default values of $C_\mu = 0.09$, $C_{1\varepsilon} = 1.44$, $C_{2\varepsilon} = 1.92$, $\sigma_k = 1.0$, and $\sigma_\varepsilon = 1.3$ were used. For the AKN simulations, the constants were adjusted to $C_{1\varepsilon} = 1.5$, $C_{2\varepsilon} = 1.9$, $\sigma_k = 1.4$, and $\sigma_\varepsilon = 1.4$ [31]. For the LR k–ω model, the damping term applied to the turbulent viscosity formulation ($\mu_t = \alpha^*\rho k/\omega$) and the vorticity production term used the following constants: $\alpha^*_\infty = 1.0$, $\mathrm{Re}_k = 6$, and $\alpha^*_0 = 0.024$. For brevity, the turbulence transport equations of the LR k–ω model are not described in detail here, but the formulation of that model can be found in Ref. [14].

Boundary Conditions. At the walls, the following nonslip BC was applied:

$$\overline{u}_i = 0, \quad k = 0, \quad \varepsilon = \nu\frac{\partial^2 k}{\partial n^2} \tag{7}$$

Periodic BCs were imposed at $x = 0$ and $x = H$

$$\begin{aligned} \overline{u}|_{x=0} &= \overline{u}|_{x=H}, \overline{v}|_{x=0} = \overline{v}|_{x=H} \\ k|_{x=0} &= k_{x=H}, \ \varepsilon|_{x=0} = \varepsilon_{x=H} \end{aligned} \tag{8}$$

At $y = 0$ and $y = H$, the symmetry BC was applied:

$$\frac{\partial\overline{u}}{\partial y} = \frac{\partial\overline{v}}{\partial y} = \frac{\partial k}{\partial y} = \frac{\partial\varepsilon}{\partial y} = 0 \tag{9}$$

The governing equations were solved by the finite volume method using the pressure-based steady solver in the FLUENT code.

Table 2 Damping functions of the ε terms used in the LRN turbulence models

Model	f_1	f_2
AKN	1	$[1-\exp(y^*/3.1)]^2[1-0.3\exp[-(R_t/6.5)^2]$
LB	$1+(0.05/f_\mu)^3$	$1-\exp(-R_t^2)$
YS	$1/[1+1/\sqrt{R_t}]$	$1/[1+1/\sqrt{R_t}]$

In all the runs, the pressure and velocity were coupled using the SIMPLE algorithm. The continuity, momentum, k, and ε equations were discretized using the second-order upwind scheme. The solutions were considered converged when the residuals of all the flow variables were smaller than 10^{-5}.

Macroscopic Modeling of Turbulence Parameters. Although the macroscopic model of the turbulence is similar to the microscopic model, the former includes two additional terms that represent the transport and production of k and ε inside the porous matrix. There are several formulations of the source terms, which are based on dimensional analysis and empirical fitting between the geometrical characteristics of the porous medium and the turbulent parameters. According to Guo et al. [32], the model presented by Nakayama and Kuwahara [18] yields better agreement with experimental results in a packed column compared to other models. Consequently, the correlations presented here are appropriate for use in this model.

As stated by Nakayama and Kuwahara, it is difficult to determine experimentally the unknown model constants, even for artificially consolidated porous media, and estimates were proposed on the basis of numerical experiments using solutions of the microscopic transport equations for k and ε [18]. By considering a macroscopically uniform flow directed along the x direction with zero mean shear and without thermal effects, the generalized macroscopic equations could be reduced to

$$\langle\overline{u}\rangle^f\frac{d\langle k\rangle^f}{dx} = -\langle\varepsilon\rangle^f + \varepsilon_\infty \tag{10}$$

$$\langle\overline{u}\rangle^f\frac{d\langle\varepsilon\rangle^f}{dx} = -C_2\frac{\left(\langle\varepsilon\rangle^f\right)^2}{\langle k\rangle^f} + C_2\frac{\varepsilon_\infty^2}{k_\infty} \tag{11}$$

For a periodically fully developed flow, the equations were further simplified to

$$k_\infty = \langle k \rangle^f \quad \text{and} \quad \varepsilon_\infty = \langle \varepsilon \rangle^f \tag{12}$$

Thus, it is possible to calculate the macroscopic model constants, k_∞ and ε_∞, from the intrinsic volume-averaged values of k and ε calculated using the microscopic governing equations under periodic and fully developed conditions. For Eqs. (10)–(12), the intrinsic volume-averaged value of a given flow variable a is obtained as

$$\langle a \rangle^f = \frac{1}{V} \int_{V_f} a dV \tag{13}$$

Grid Independence Analysis. The grid independence was verified, taking as representative the case of the most highly confined flow (DR = 0.8 and $\phi = 0.27$) under fully turbulent conditions ($\mathrm{Re}_D = 100 \times 10^3$), and the STD model. As shown in Table 3, four grids with cell sizes ranging from 16×10^3 to 127×10^3 were constructed by halving the total grid size. To avoid false spatial convergence, especially in the near-wall region, the number of nodes N arranged uniformly along each cylinder wall was sequentially doubled. In addition, the near-wall regions were highly refined to capture the strong flow gradients resulting from the nonslip condition. During the meshing process, a fixed number of nodes were imposed along the walls of the smallest cylinders, as well as at the periodic and symmetric edges. All the edges were connected by the proximity and curvature algorithm using a growth rate of 1.20. The average skewness values of the resulting grids were less than 0.08. According to the ANSYS meshing guidelines, grids with average skewness values of less than 0.1 are of high quality [33].

The vorticity (ω) is an important indicator of flow rotation and requires good predictions of the velocity gradients. In addition, ε is related to the kinetic energy lost to viscous dissipation. Figs. 3(*a*) and 3(*b*) show the profiles of the dimensionless ω and ε values extracted at the vertical line L_1 located $0.1H$ from the periodic left edge (see Fig. 4). Because this line appears in a region where high flow gradients are present, it was considered suitable for comparison.

Because of the gap flow, the profiles of the dimensionless ω and ε values are asymmetric. The shapes of the profiles are similar regardless of the number of cells. However, the level of refinement appeared to affect the magnitude of the values, especially in the 33.3 k and 60.4 k grids. The vorticity of these grids showed a maximum deviation of 16% at $y/L_1 = 0.5$, whereas the predicted values of ε deviated by approximately 15% at $y/L_1 = 0.4$. At the next-highest level of refinement, the profiles corresponding to the 60.4 k and 127 k grids were very similar, and the maximum differences in the values of vorticity and ε at the same location decreased to approximately 4.6% and 3.3%, respectively.

The predicted volume-averaged values of the dimensionless k and ε are listed in Table 3. The grid convergence indexes (GCIs) and extrapolated errors (e_{ext}) were estimated by comparing the predictions with the values obtained using the Richardson extrapolation method following the methodology for nonuniform grids presented in Celik and Karaketin [34]. The extrapolated errors between the 60.4 k and 127 k grids were 0.31% and 0.11% for k and ε, and their GCIs were 0.93% and 0.36%, respectively. These differences are in fair agreement with those in other numerical works [16,35].

Table 3 Cell numbers and dimensionless volume averaged k and ε for the different grids

	# Cells	N	$\langle k \rangle^f / u_D^2$	$\langle \varepsilon \rangle^f H / u_D^3$
STD model	16,024	80	1.261	69.02
$\mathrm{Re}_D = 1 \times 10^5$,	33,298	140	1.252	73.79
$\phi = 0.27$	60,442	250	1.260	78.82
DR = 0.8.	126,962	500	1.247	79.14
	Extrapolated	—	1.256	78.92
	e_{ext}	—	0.31 %	0.11%
	GCI	—	0.93 %	0.36%

Because damping functions act in the near-wall regions where viscous effects are important, two additional grids with lower y^+ values were tested using the AKN model. In the first refinement, 1000 nodes were placed along each cylinder wall using the grid characteristics explained above. A further increase to 2000 nodes was applied in the second refinement, resulting in a 411k grid. The cell numbers and y^+ values of those grids are shown in Table 4. No important differences were found in the main velocities and turbulence parameters. As an example, the turbulent kinetic energy profiles obtained at the line L_1 are shown in Fig. 3(*c*). The volume-averaged k values in Table 4 differed by less than 2% between the coarsest and finest grids. Thus, because the 60.4 k grid predictions were in good agreement with those of larger grids but required less computational time, that grid was selected as the outline to perform the rest of the simulations. The nodal distribution of the selected grid is shown in Fig. 4. The total number of cells in this grid is consistent with those used in other works [19–21].

Results and Discussion

Analysis of the Low-Reynolds-Number Turbulence Models (Reynolds Number Effect). The relationship between DR and the flow characteristics has been further analyzed using the most satisfactory LRN turbulence model. The intrinsic volume-averaged values of k and ε predicted by each model are shown in Figs. 5(*a*) and 5(*b*). Because no studies were found in which DR was varied, the base case corresponds to the flow over a staggered arrangement of square cylinders at $\phi = 0.3$ and DR = 1.0. The corresponding RVE is shown in the inset of Fig. 5(*a*). Here, Re_D was varied from 500 to 4×10^4 to compare our results with those of similar works.

At $\mathrm{Re}_D = 500$, the values predicted by the LRN turbulence models were scattered. At this Reynolds number, the YS model delivered the lowest values. For k, the AKN and LR k–ω models showed fair agreement with the results of Kundu et al. [21], whereas the LB and STD responses were closer to the values of Kuwahara et al. [11]. For the turbulent kinetic energy dissipation rate, the results of the LR k–ω model were in good agreement with the data from Kundu et al., whereas the STD model response was greatly overestimated. When Re_D was increased further (ReD> 1000), the inertial forces were even more dominant. In this case, the k values predicted by the LB model decreased from the maximum value of approximately $\langle k \rangle^f / u_D^2 = 5.0$ at $\mathrm{Re}_D = 1 \times 10^3$ to $\langle k \rangle^f / u_D^2 = 2.4$ at $\mathrm{Re}_D = 4 \times 10^4$. The results of the other LRN turbulence models and the STD model were independent of Re_D, and the magnitudes were almost constant. For the LR k–ω and YS models, the dimensionless k values were poorly predicted, whereas those of the AKN and STD models were in good agreement with those reported in other works. The LB and AKN models predicted constant values of the dimensionless ε independent of Re_D, and the values of the YS and LR k–ω models were slightly below those reported by Kundu et al. [21] and Teruel and Rizwan-Uddin [36]. Except for $\mathrm{Re}_D = 1 \times 10^3$, the STD model showed good agreement with the other works. The differences between the LRN turbulence models, STD model, and LES at $\mathrm{Re}_D = 500$ may be related to transitional flow effects, because Re_D is near the reported limit for the onset of turbulence, $\mathrm{Re}_D = 300$ [37]. However, further studies are needed to elucidate these differences.

Figure 6 shows the behavior of the dimensionless MPG predicted by the models as a function of Re_D. The AKN, STD, and YS values of this parameter were consistent with the linear tendency reported by Kundu et al. [21] and Kuwahara et al. [11].

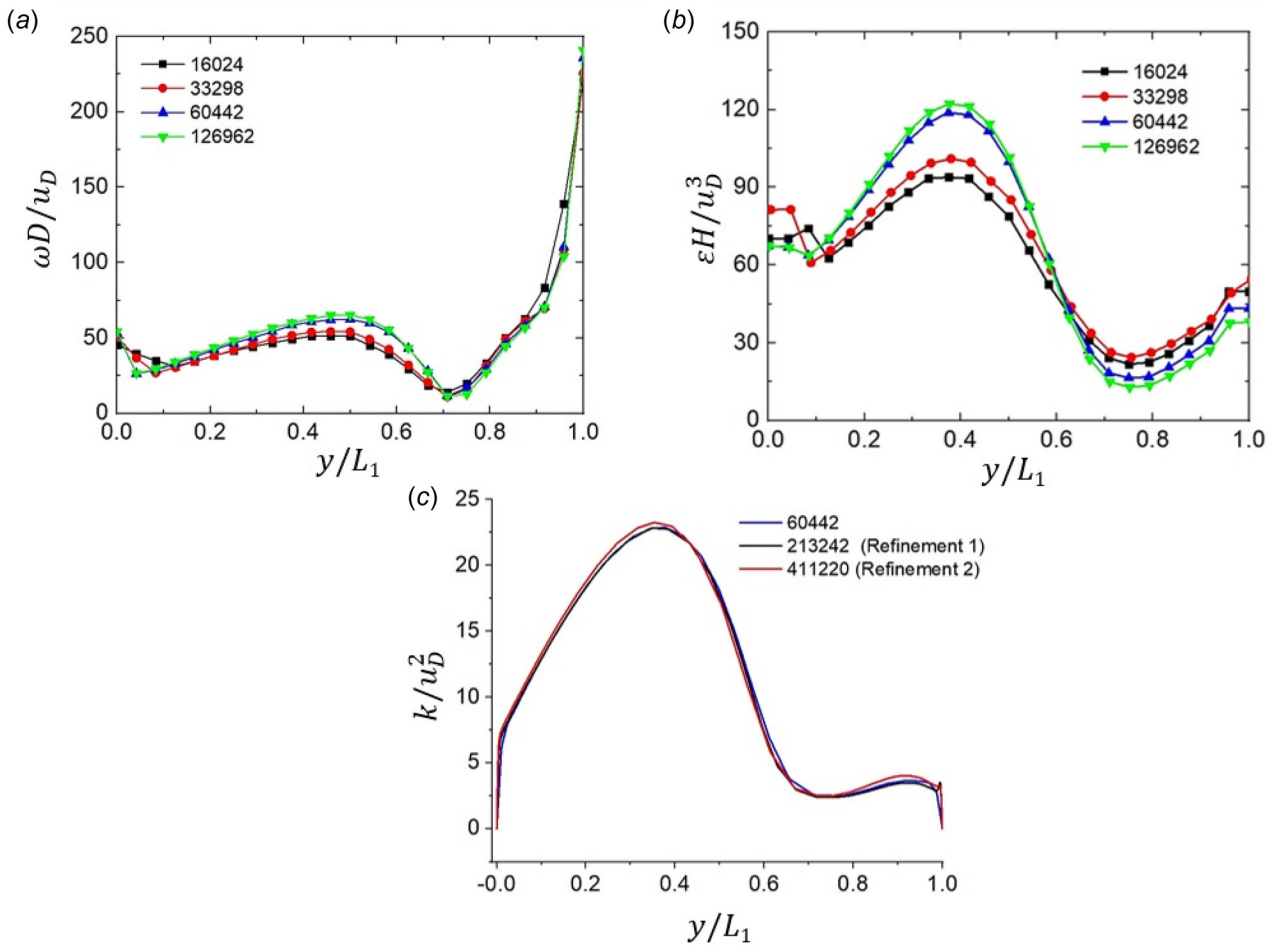

Fig. 3 Comparison of profiles for grid independence analysis, and the effect of the near-wall refinement: (*a*) mean vorticity magnitude at L_1, (*b*) dimensionless ε at the line L_1, and (*c*) effect of the near-wall resolution in terms of k at the line L_1

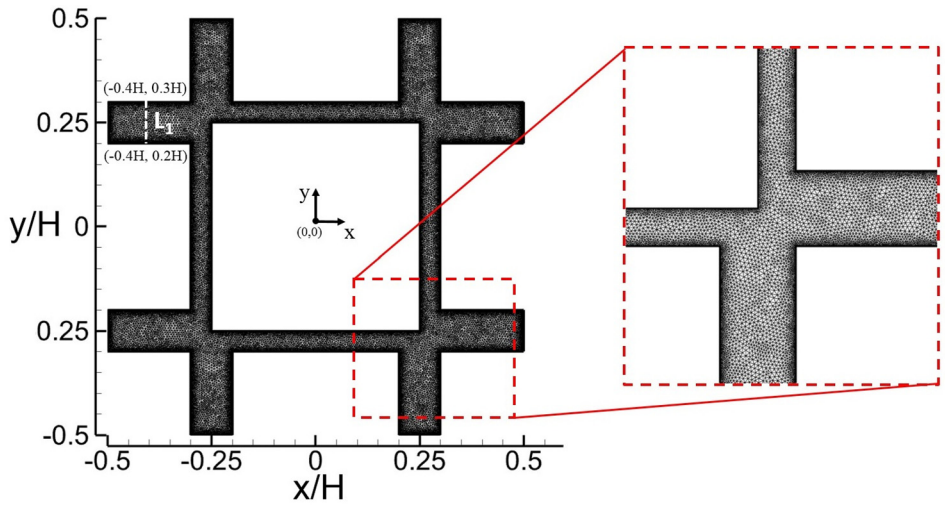

Fig. 4 Detail of the final grid used as basis to all the final simulations

Although the LB and LR k–ω models gave slightly over-and under-estimated values, respectively, both models could also be considered to be in fair agreement with the other works. In summary, when Re_D was near the onset of turbulence, the results of the models showed significant differences in k and ε. At higher Re_D, both turbulence parameters tended to be constant, and the AKN and STD models were in better agreement with other data from the literature. For k in particular, the YS and k–ω LRN models underestimated the values. All the assessed models showed reasonable results for the MPG.

Volume-Averaged Values as a Function of ϕ Predicted by the Low-Reynolds-Number Turbulence Models. The turbulence parameters and macroscopic pressure gradient as a function

Table 4 Effect of the grid resolution in the near-wall regions at $Re_D = 100 \times 10^3$, $\phi = 0.27$ and DR = 0.8

#Cells	N	y^+	$\langle k \rangle^f / u_D^2$
60,442[a] (Base grid)	250	20.79	1.035
213,242[a] (Refinement 1)	1000	5.73	1.030
411,220[a] (Refinement 2)	2000	2.99	1.048
411220[b] (Refinement 2)	2000	2.97	1.031

[a]AKN model.
[b]YS model.

of ϕ were evaluated. For this purpose, the dimensions of the RVE composed of square cylinders with DR = 1.0 were changed according to the relation $\phi = 1 - (D/H)^2$ to cover a porosity range of 0.3–0.8 in intervals of 0.1. The runs were performed at $Re_D = 50 \times 10^3$, representing fully turbulent flow conditions. The dimensionless k and ε results are shown in Figs. 7(*a*) and 7(*b*), respectively. For comparison, the correlation formulas suggested by Nakayama and Kuwahara [18] and data from other authors are also included.

As shown in Fig. 7(*a*), the LB model overestimated the values of k, whereas the YS and LR k–ω models underestimated them. Both the AKN and STD models showed fair agreement with Yang et al. [16] and Nakayama and Kuwahara [18]. The differences between the RANS predictions of Nakayama and Kuwahara, and those obtained by LES, are attributed to the overestimation of the production of the k term, especially in regions where the flow is strongly decelerated, as discussed in [11]. Although the LES model is better able to avoid this disadvantage, as discussed above, it also requires significant computational resources.

The turbulent dissipation rates predicted by the STD, AKN, LB, and YS models were in good agreement with those reported in other works, and the LR k–ω model underestimated the values. No information related to this turbulence quantity by more powerful approaches such as LES was found in the literature. The dimensionless MPG as a function of ϕ is shown in Fig. 8. For comparison, the correlation formulas of Nakayama and Kuwahara [18] and Kundu et al. [21] are also plotted. For this parameter, all the assessed models showed the nonlinear tendency suggested by Kundu et al. and were in agreement with the LES results of Kuwahara et al. [11]. According to Kundu et al., this loss of linearity at $(1-\phi)/\phi^3 > 2$ is related to slower growth of the friction factor compared to that at higher porosity, where different flow patterns within pores also appear [21].

Overview of the Source of Differences Between the Low-Reynolds-Number Turbulence Models. Some insights about the source of the differences between the volume-averaged quantities

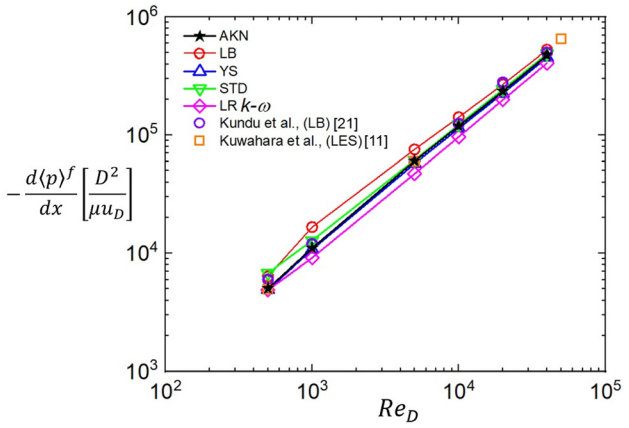

Fig. 6 Response of the macroscopic pressure gradient as a function of Re_D for the tested models

predicted by the LRN turbulence models are presented. The formulation of the LR k–ω model was intended to capture the main features of a flat-plate boundary layer during a transition from laminar to turbulent flow [14]. This goal was realized by including a damping function in the eddy viscosity term α^*, and the damping β^* term, accounted for, in its turbulent kinetic energy dissipation rate definition ($\varepsilon = \beta^* k\omega$). These functions were formulated so as to meet the following conditions: (a) The critical Reynolds number (Re_{xc}) at which production overcomes dissipation in the k equation matches the minimum Re_{xc} at which Tollmien–Schlichting waves begin to form; (b) The asymptotic behavior of k and ε as they approach a solid boundary is verified; and (c) the closure constants preserve their original fully turbulent values at $Re_{t\omega} \to \infty$. According to our results, this model delivered reasonable values for k at the lowest Re_D value of 500 because its formulation accounts for transitional features. However, at higher Re_D, both k and ε were underestimated, suggesting that excessive damping occurs in fully turbulent flow.

The differences between the results of the LB model and the literature data can be explained by considering that the validity of the damping functions and inner constants were verified in fully developed pipe flows without pressure gradient effects. According to Abe et al. [24], the LB model fails to reproduce the near-wall limiting behavior of the Reynolds stresses. In addition, those authors also reported differences in the friction coefficient of a flow affected by an adverse pressure gradient.

Although the damping functions employed in the YS model were validated using data from flat-plate boundary layers, channel

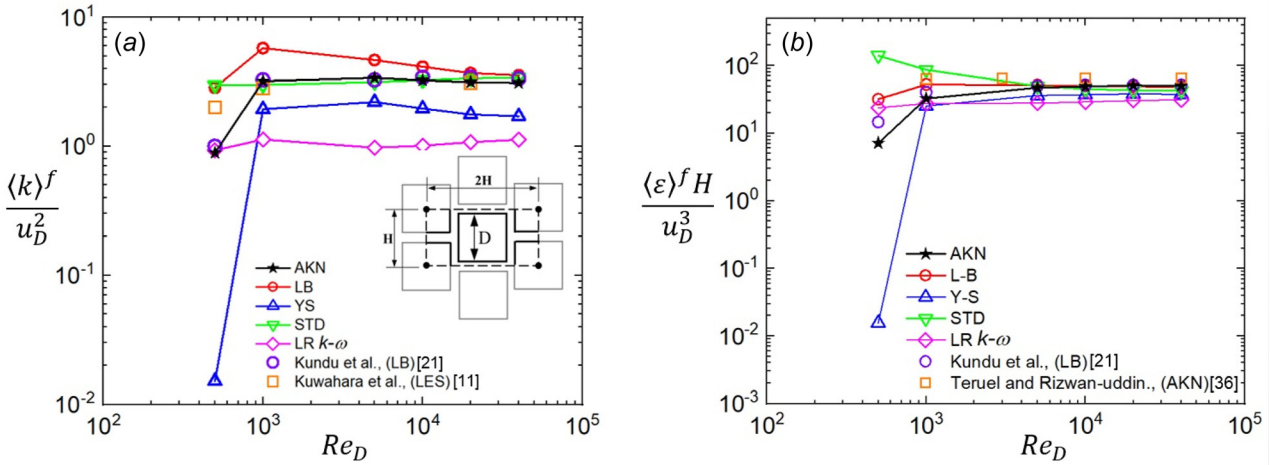

Fig. 5 Numerical response of the assessed LRN turbulence models as a function of Re_D: (*a*) dimensionless turbulent kinetic energy and (*b*) dimensionless turbulent kinetic energy dissipation rate

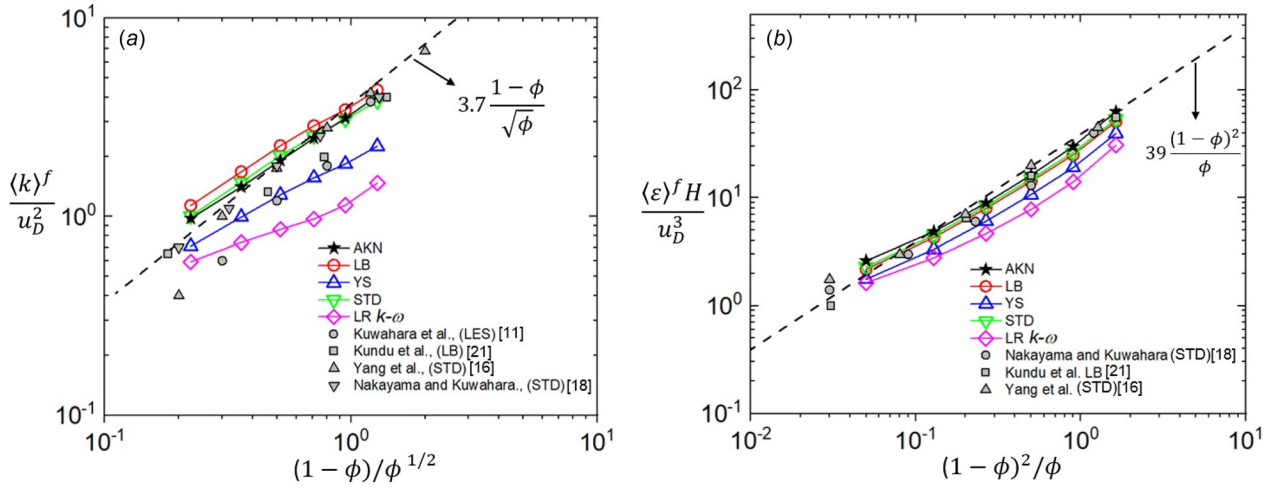

Fig. 7 Turbulence parameters as a function of porosity: (*a*) dimensionless turbulent kinetic energy and (*b*) turbulent kinetic energy dissipation rate

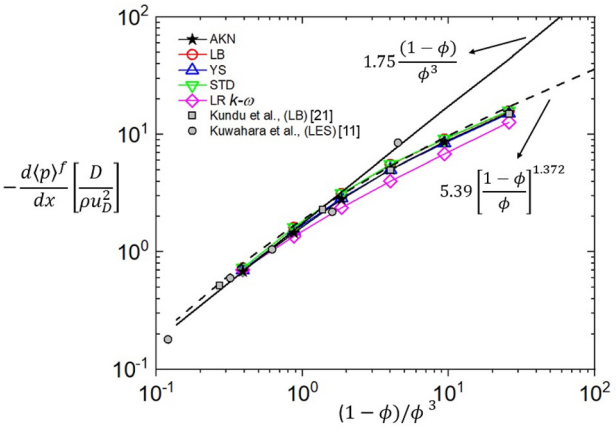

Fig. 8 Effect of ϕ on the macroscopic pressure gradient over an arrangement of square cylinders with the same diameter

flows, and flows under the influence of an adverse pressure gradient, the volume-averaged k values obtained here were underestimated when they were evaluated as a function of Re_D or ϕ. To better understand the source of this underestimation, the response of the YS model was evaluated using a refined grid of 411k cells at $\phi = 0.27$, DR = 0.8, and $\mathrm{Re}_D = 100 \times 10^3$. As shown in the last row of Table 4, the predicted volume-averaged k values showed better agreement with those of the AKN model, suggesting that the YS model depends strongly on near-wall refinement. This suggestion is reasonable considering that the intrinsic volume-averaged results rely on the numerical integration of the cell values along the entire domain. However, a comparison of the k profiles obtained for the flat-plate and adverse pressure gradient test cases by Yang and Shih [25] reveals that discrepancies occurred, most of which were underestimations in the inner layer region. In addition, in the work of Hrenya et al. [10], the YS model underestimated the axial velocity in the logarithmic region of a turbulent pipe flow at $\mathrm{Re} = 7 \times 10^3$ and underestimated k at some near-wall locations as Re was increased to $\mathrm{Re} = 500 \times 10^3$.

In the formulation of the AKN model, the functions were designed to deal mainly with separating and reattaching flows, and the Kolmogorov velocity scale was used to account for near-wall damping of the Reynolds stresses. This model predicted the friction factor, mean velocities, separation–reattachment length, and turbulence quantities in a backward-facing step well [24]. Because the flow features are expected to be defined by flow separation and reattachment in simulations with different DR and ϕ values, the AKN model was used in additional runs.

Description of the Volume-Averaged Flow Parameters as a Function of $\mathrm{Re_D}$ and Diameter Ratio. The dimensionless volume-averaged ω, k, ε, and MPG plotted as a function of DR and Re_D are shown in Figs. 9(*a*)–9(*d*). In all these runs, a fixed RVE height H was used. As shown in Fig. 9(*a*), the vorticity is almost constant in the entire Re_D range. At the lowest DR = 0.2 value and the highest porosity of $\phi = 0.72$, the flow is less bounded, and the vorticity values are the lowest. From the minimum value of $\omega = 10$, the value increased in proportion to DR, reaching a maximum of $\omega = 100$ at DR = 0.8 and $\phi = 0.27$. Although the DR = 0.8 and DR = 1.0 domains had similar porosity values, the volume-averaged vorticity in the pores at DR = 0.8 was almost twice that at DR = 1.0.

Except for the base case, the turbulent kinetic energy increased significantly between $\mathrm{Re}_D = 500$ and $\mathrm{Re}_D = 1 \times 10^3$. For $\mathrm{Re}_D > 1 \times 10^3$, the turbulent kinetic energy was almost constant in all the pore models. The values of k inside the pore domains were similar at DR = 0.2 and 0.4 and increased dramatically at DR = 0.8. The base case delivered more k than the DR = 0.8 case, in contrast to its predictions for ω.

The turbulent kinetic energy dissipation rate results are shown in Fig. 9(*c*). Again, a sharp increase appeared between $\mathrm{Re}_D = 500$ and $\mathrm{Re}_D = 1 \times 10^3$, and the values tended to be constant at higher Re_D. However, for this parameter, between DR = 0.2 and DR = 0.4, the magnitudes increased, and the largest values, which exceeded those of the base case, appeared for the DR = 0.8 model. The MPG of the models grew linearly as a function of Re_D. In addition, the DR = 0.8 and the base case values were very similar. No large differences appeared between the DR = 0.2 and DR = 0.4 models, and the values for DR = 0.6 were intermediate between those of these two models.

The independence of the volume-averaged values of k and ε in fully turbulent flow (i.e., at $\mathrm{Re}_D > 1 \times 10^3$) were reported by [16,18,21] for regular domains composed of particles with the same D, and it was preserved even when DR varied. As will be explained below using maps of the interstitial velocity, vorticity, and turbulence, the values of the volume-averaged k, ε, and ω in terms of DR, are related to peculiar shear layer interactions, recirculation regions, and flow streams that formed between cylinders as their wall distances changed.

Assessment of the Flow Patterns Formed at Different Diameter Ratio. To investigate the local flow structures inside the porous media, which determine the volume-averaged values, contour maps of the dimensionless mean velocity and vorticity obtained at different DR values in fully turbulent flow

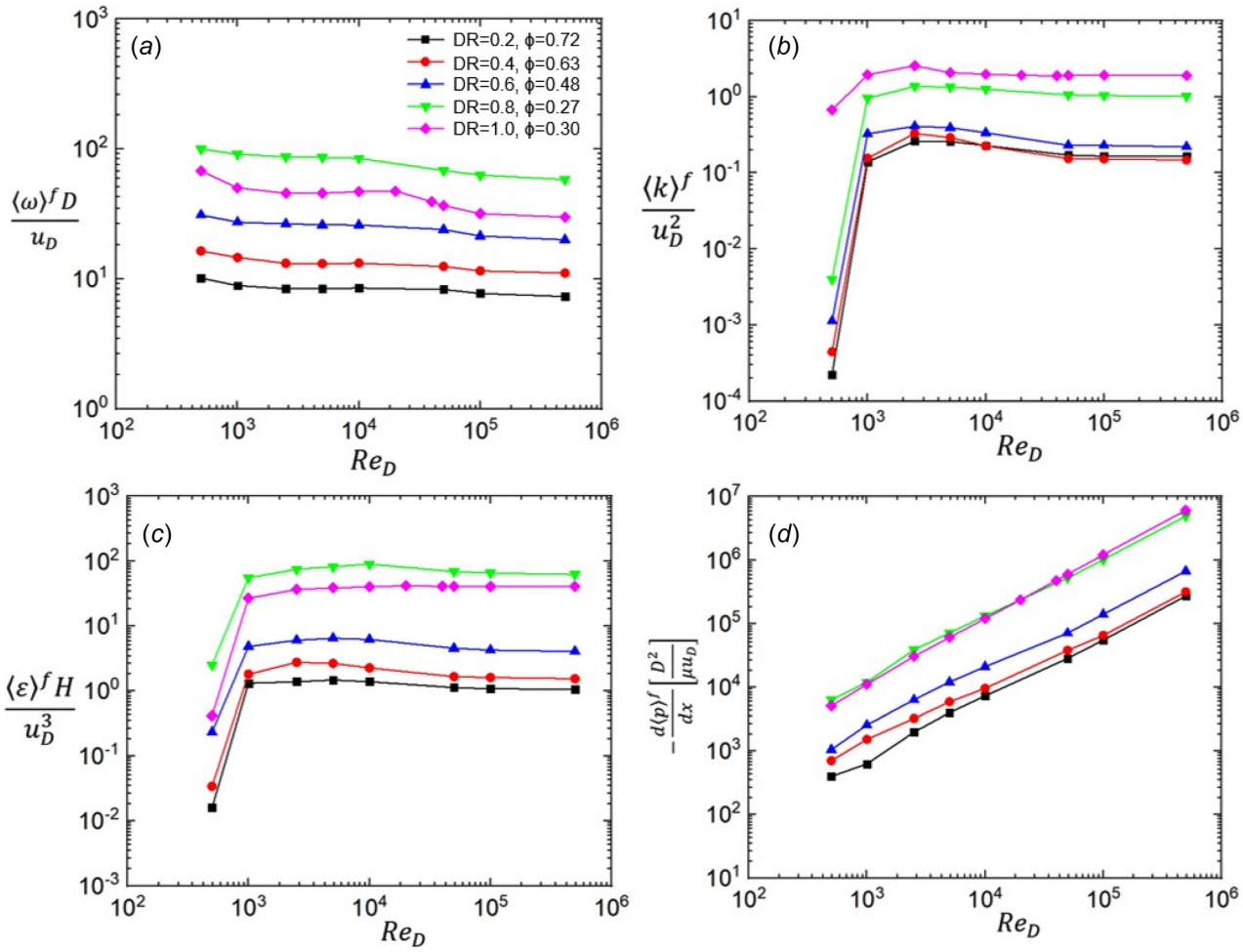

Fig. 9 Dimensionless intrinsic volume averaged quantities as a function of Re_D and DR: (*a*) vorticity magnitude, (*b*) turbulent kinetic energy, (*c*) turbulent kinetic energy dissipation rate, and (*d*) macroscopic pressure gradient

($Re_D = 50 \times 10^3$) are presented in Fig. 10. As reported in the Description of the Volume-Averaged Flow Parameters as a Function of Re_D and Diameter Ratio section, the volume-averaged values of most of the variables were similar in the DR = 0.2 and DR = 0.4 models. Therefore, the DR = 0.4 contour maps are not included in this analysis.

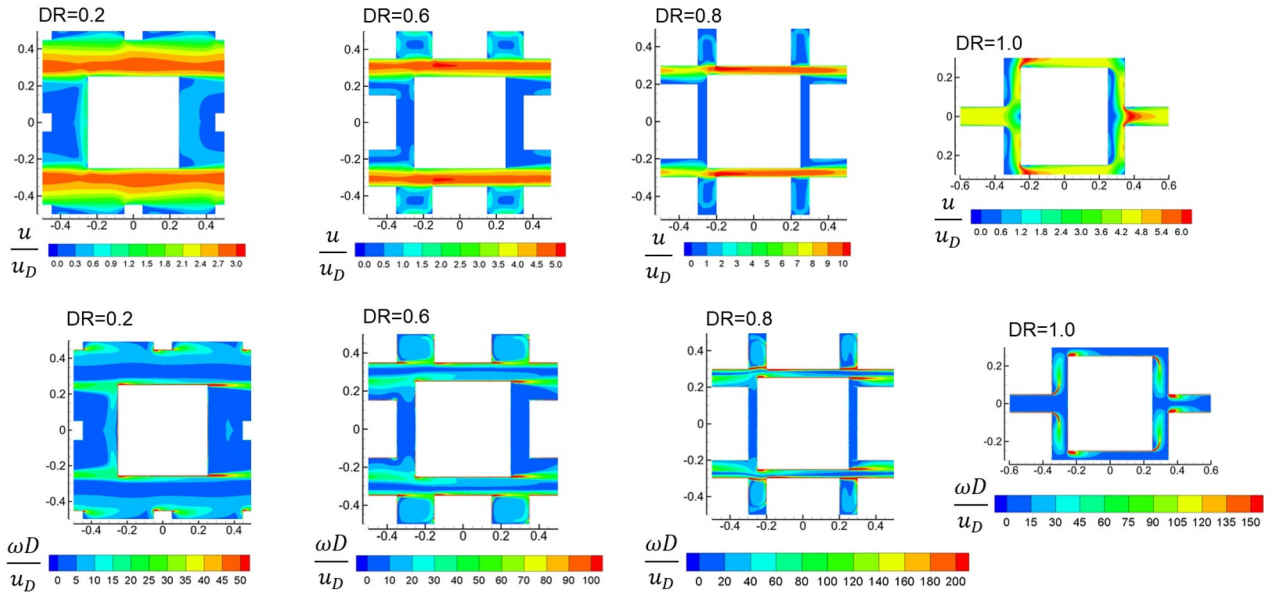

Fig. 10 Contour maps of dimensionless velocity and vorticity for different DR at $Re_D = 50 \times 10^3$. Axis in figures are *x*/*H* and *y*/*H*.

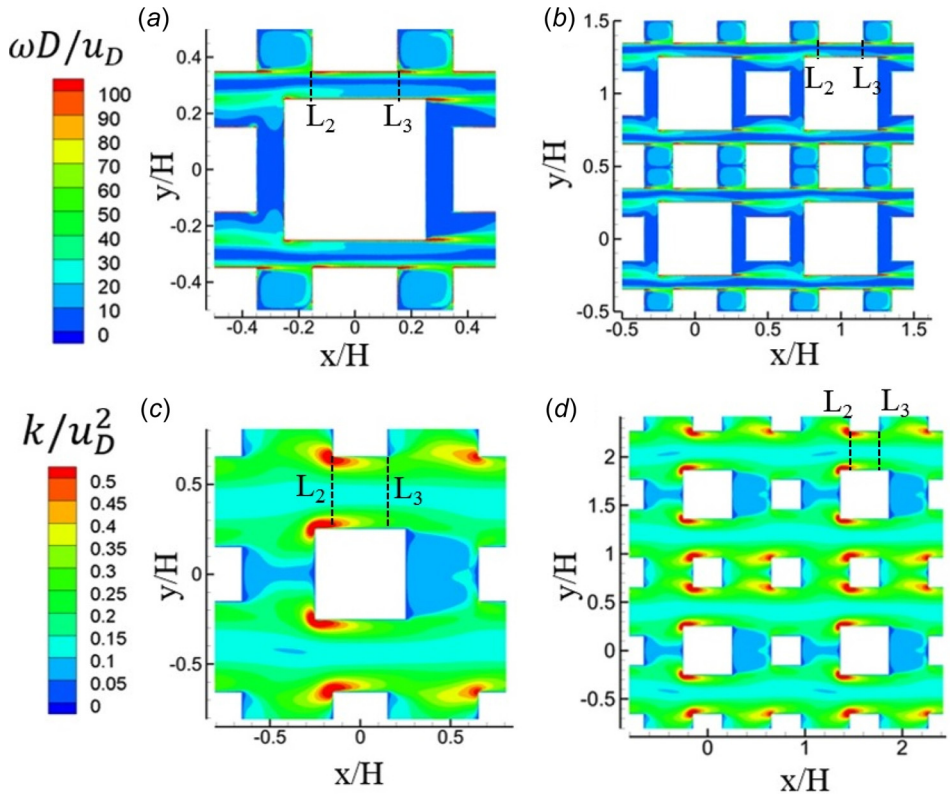

Fig. 11 Effect of increasing the number of repetitive elements in the RVE's: (*a*) periodic domain composed of one large cylinder arrangement, simulated at Re_D=50 × 10^3, DR = 0.6 and ϕ=0.48, (*b*) domain composed of four large cylinders, at Re_D = 50 × 10^3, DR = 0.6, and ϕ=0.48, (*c*) one large cylinder arrangement tested at Re_D = 5 × 10^3, ϕ=0.8 and DR = 0.6, and (*d*) RVE composed of four large cylinders at Re_D=5 × 10^3, ϕ=0.8, and DR = 0.6

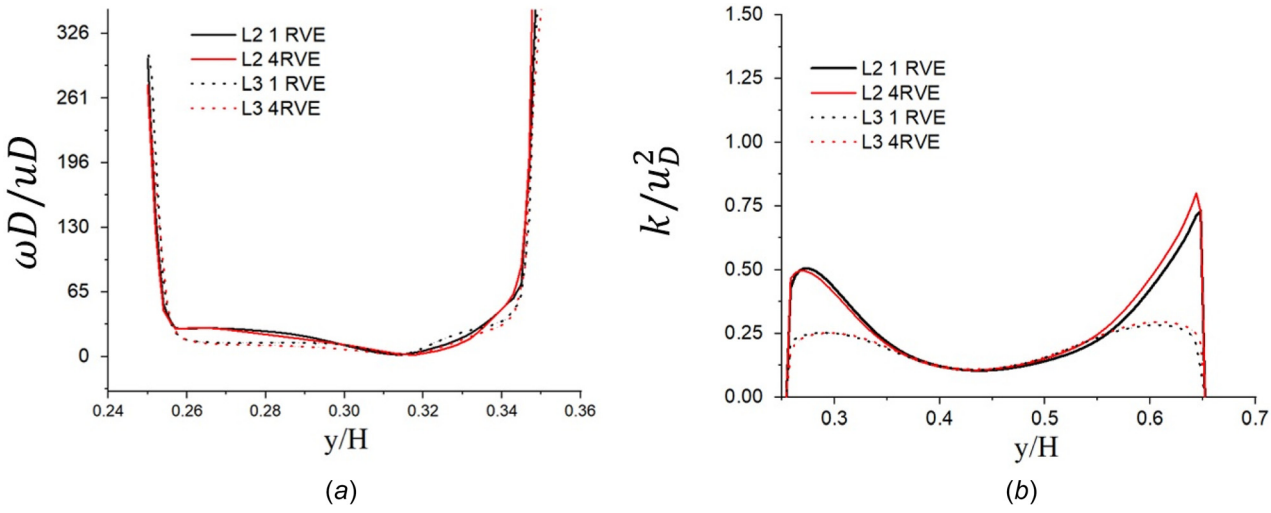

Fig. 12 Comparison of the profiles of vorticity and *k* extracted from the lines L_2 and L_3 shown in Fig. 11: (*a*) results for the case corresponding to Re_D = 50 × 10^3, DR = 0.6 and ϕ=0.48 and (*b*) results corresponding to the case Re_D = 5 × 10^3, ϕ = 0.8, and DR = 0.6

At the lowest DR value of 0.2, two well-defined high-velocity streams with maximum velocity of $u/u_D = 2.8$ appeared in the upper and lower parts of the large square. For the domains corresponding to DR = 0.6 and 0.8, the maximum velocity increased by a factor of approximately two, as the flow confinement increased. In the upper and lower vertical flow channels between the small cylinders, and in the space between the large- and small-centered cylinders, the flow velocities were low. Interestingly, the velocity exhibited very different behavior in the base case compared to the other arrangements, because the main flow stream impinged directly upon the main square. This result indicates the effect of particle sorting on the mean flow patterns.

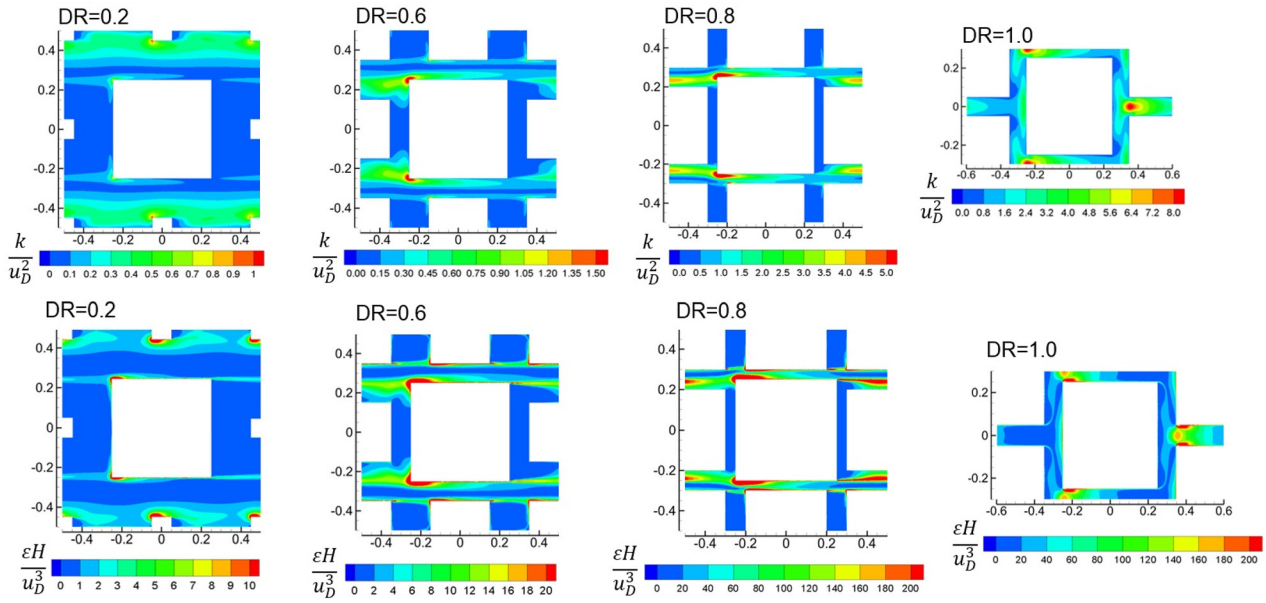

Fig. 13 Contour maps of the dimensionless turbulent kinetic energy and its dissipation rate at different DR at Re_D=50 × 10^3. Axis in figures are *x*/*H* and *y*/*H*.

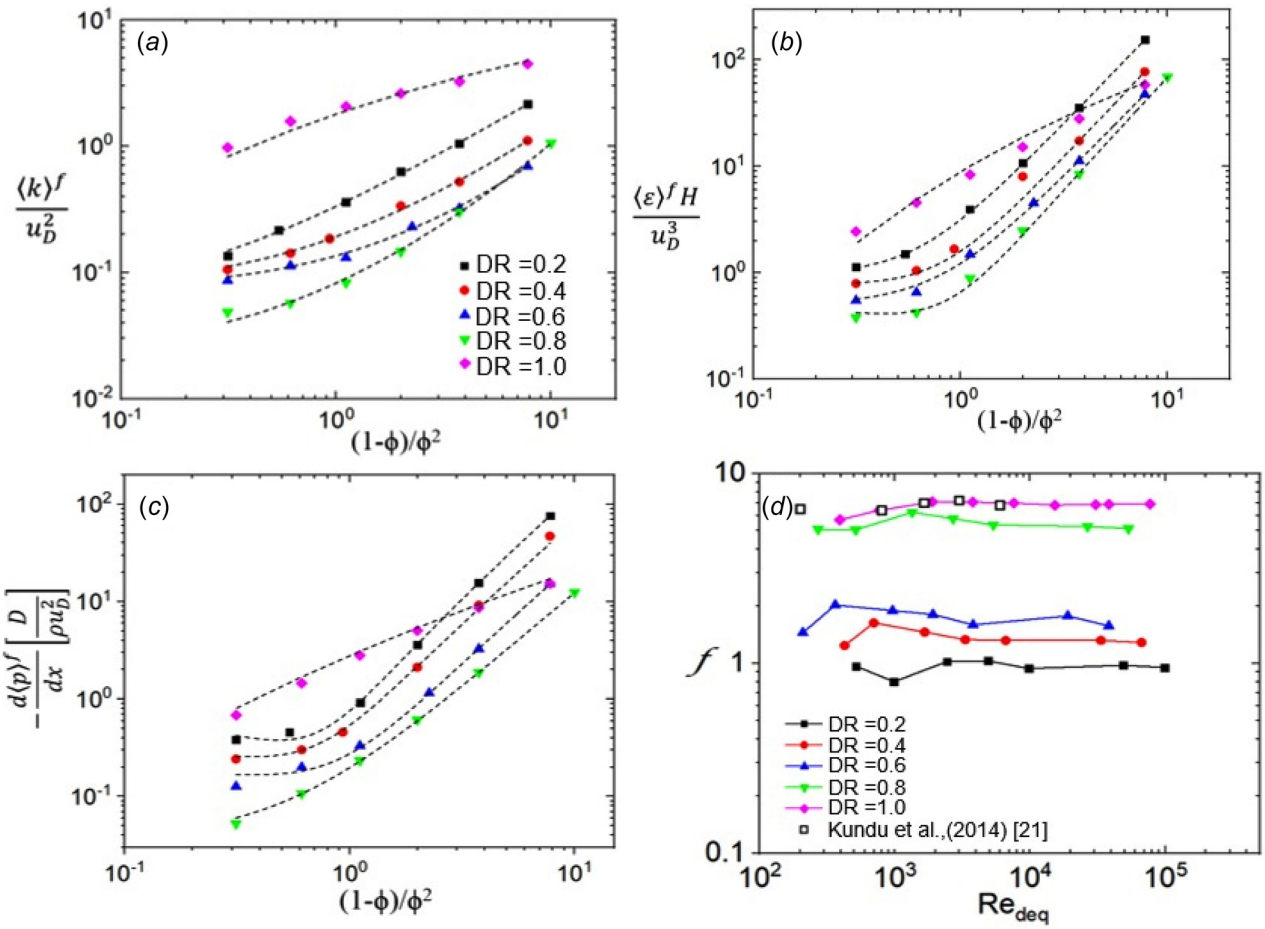

Fig. 14 Volume averaged flow parameters as a function of porosity: (*a*) *k*, (*b*) ε, (*c*) MPG, and (*d*) friction factor for cases where *H* is fixed (dashed lines are the correlation functions)

Owing to interaction between the walls and the main flow streams, distinctive vortical structures appeared. For the DR = 0.2 configuration, two symmetrical and well-defined shear layers of high vorticity ($\omega D/u_D = 25$–50) appeared behind the smaller cylinders. No important high-vorticity spots were present between the main cylinder and the two smaller centered ones. At DR = 0.6,

Table 5 Adjustment constants *A*, *B*, and *C* for the polynomial approximation proposed for the different DR models

DR	*A*	*B*	*C*	R^2
$\langle k \rangle^f / u_D^2$				
0.2	0.065	0.269	-1.24×10^{-4}	0.9996
0.4	0.076	0.114	2.32×10^{-3}	0.9988
0.6	0.073	0.060	2.41×10^{-3}	0.9968
0.8	0.023	0.055	4.84×10^{-3}	0.9997
$\langle \varepsilon \rangle^f H / u_D^3$				
0.2	1.171	−0.565	2.617	0.9998
0.4	0.863	−0.610	1.345	0.9998
0.6	0.513	−0.081	0.793	0.9998
0.8	0.546	−0.631	0.744	0.9998
$-\frac{d\langle p \rangle^f}{dx}\left[\frac{D}{\rho u_D^2}\right]$				
0.2	0.714	−1.377	1.423	0.9998
0.4	0.357	0.536	0.721	0.9998
0.6	0.204	−0.202	0.273	0.9998
0.8	0.035	0.044	0.119	0.9998

the maximum vorticity reached 100 units, and the shear layers that formed behind the upper and lower cylinder rows were disrupted by the presence of the wall. Consequently, two rotating flow zones of $\omega D/u_D = 10$–40 were formed inside the vertical gaps.

At the highest DR value of 0.8 and the lowest porosity, the vorticity increased further to $\omega D/u_D = 200$. Because the vortical regions in the upper and lower vertical gaps were plugged by the shear layers of the smaller cylinders, their vorticity magnitude did not change significantly. Similar shear layers and high-velocity streams have been observed experimentally in domains consisting of aligned cylinders with the same diameter by Larsson et al. [38] and numerically in the transitional regime by Agnaou et al. [39].

To verify the validity of the vortical regions trapped inside the upper and lower gaps, an additional run using an RVE four times larger than the original one was conducted for DR = 0.6 and $\phi = 0.48$. As shown in Figs. 11(*a*) and 11(*b*), the results for these two RVE sizes were nearly identical. An additional analysis was conducted at a lower Re_D of 5×10^3 for the highest porosity ($\phi = 0.8$) and the same DR. As shown in the contour maps of the dimensionless k in Figs. 11(*c*) and 11(*d*), the predictions for each RVE size were again very similar. Figure 12 compares the predicted profiles in regions where strong flow gradients are present

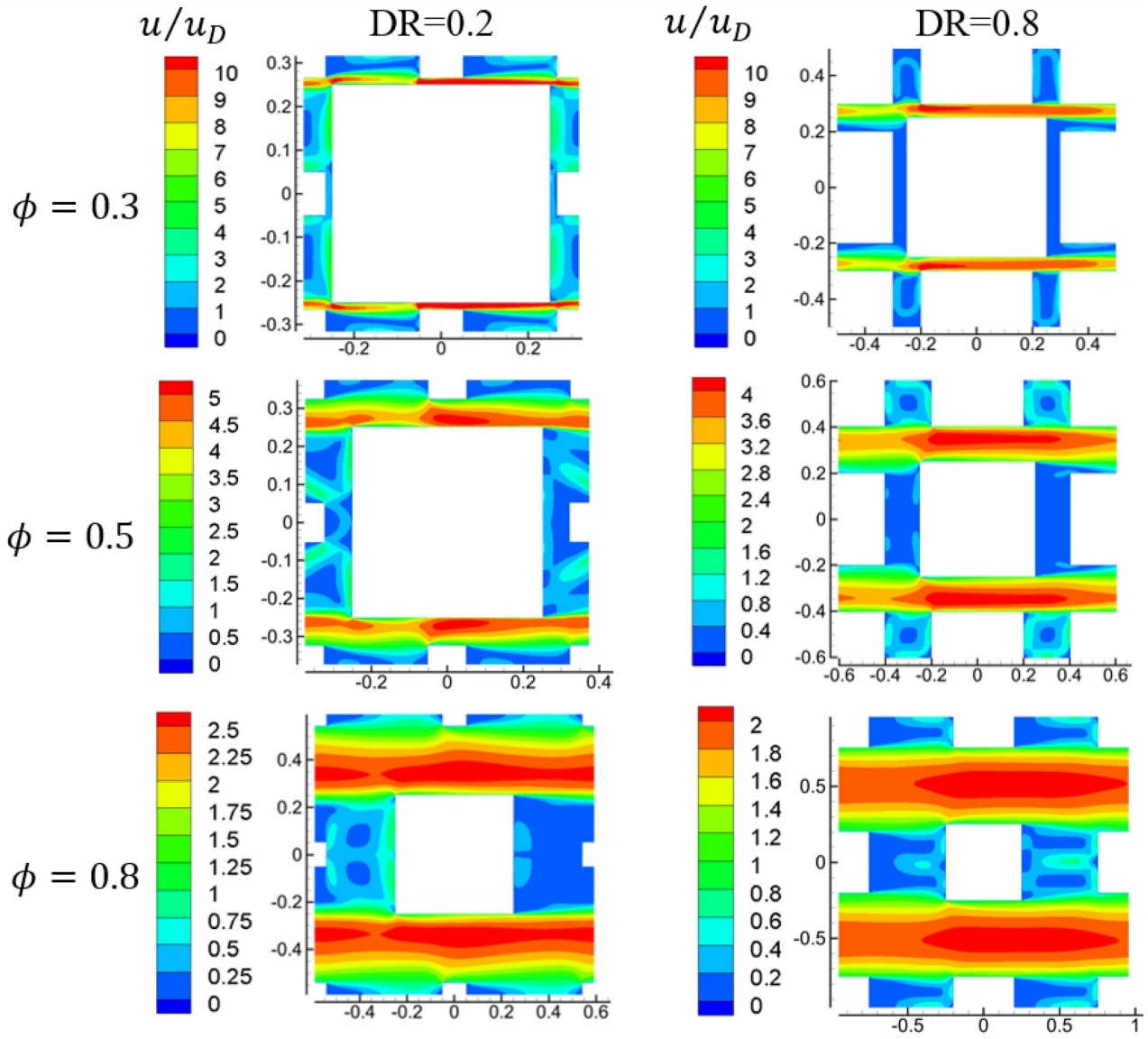

Fig. 15 Contours of dimensionless mean velocity as a function of ϕ and DR at $\mathrm{Re}_D = 50 \times 10^3$. Axis in figure are *x*/*H* and *y*/*H*.

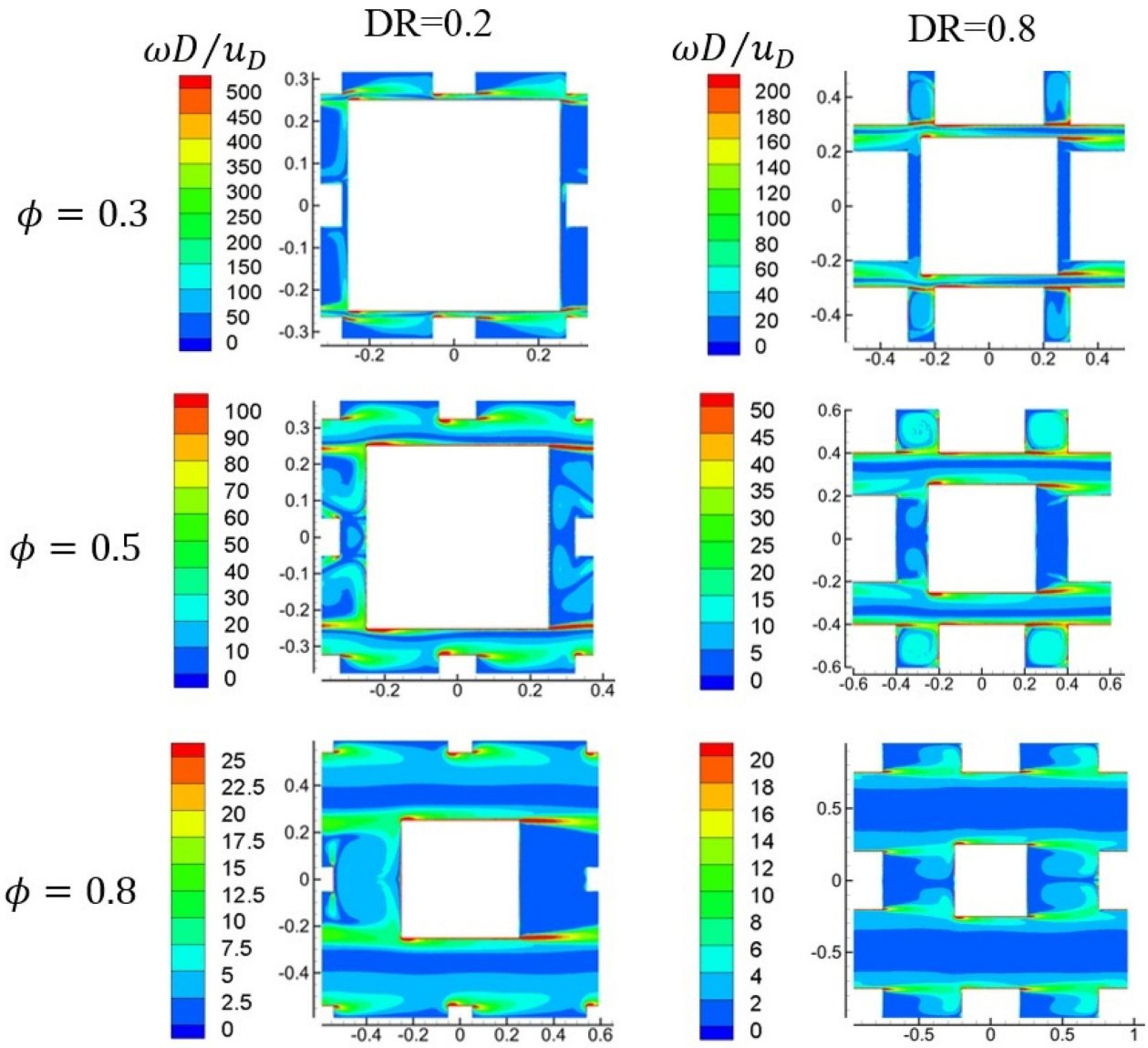

Fig. 16 Contours of vorticity as a function of ϕ and DR at $Re_D = 50 \times 10^3$. Axis in figure are *x/H* and *y/H*.

(lines L_2 and L_3 in Fig. 11). Again, good agreement was obtained in all the cases. In addition, a DNS of a porous medium consisting of an array of cylinders with the same D at high porosity ($\phi > 0.75$) showed that the turbulence structures are generally limited by the pore size [6]. Furthermore, even when the structures are extended and have a slight effect on nearby pores, this effect decays with distance, and no large-scale structures are expected to persist [5].

The local mean distributions of the dimensionless k for different DR values are shown in Fig. 13. For DR = 0.2, uniform values of approximately $k/u_D^2 = 0.5$–0.7 were observed between the smaller cylinders, with barely visible regions of $k/u_D^2 = 1.0$ at their front edges.

By contrast, for DR = 0.6, the gradients were more intense, but k was less sparse within the domain. The highest value, $k/u_D^2 = 1.5$, appeared at the corners of the front edge of the large cylinder. In the upper vertical channels as well as the lateral side channels between the centered cylinders, the k values were low. The k patterns for DR = 0.6 and 0.8 did not differ significantly. However, for DR = 0.8, the maximum value was $k/u_D^2 = 5.0$, which is at least three times the values in the DR = 0.6 case.

The values of the turbulent dissipation rate depended strongly on DR. For DR = 0.2, zones in which the turbulent dissipation rate had a maximum value of $\varepsilon H/u_D^3 = 10$ appeared at the front corners of the large cylinders as well as in the upper faces of the smaller ones. In the rear parts of the smaller cylinders, some gradients of ε with intermediate values were observed. As the flow became more confined, the turbulent dissipation rate increased, and the zones with higher gradients were relocated such that they almost coincided with those of high k. The maximum levels of turbulent dissipation rate appeared for DR = 0.8, where $\varepsilon H/u_D^3 = 200$, which is approximately 20 times the values for DR = 0.2. Because the turbulent dissipation rate is related to the energy loss due to viscous effects, this result suggests that the major contributor to the flow energy losses is dissipation in the walls by friction for DR = 0.6 and 0.8. For DR = 0.2, turbulent dissipation rate gradients were observed in the shear layers of the smaller cylinders. Delafosse et al. [40] have reported that the regions of high ω, k, and ε are close to each other, and this observation has been explained by considering that inside the vortex cores, the turbulent kinetic energy is maximum, and thus, the turbulent dissipation rate has been linked to nearby positions. The flow patterns of k and ε in the base case were notably different from those in the other configurations. The regions with high gradients of the turbulent kinetic energy and its dissipation rate coincided with the high-velocity core region, but not with the

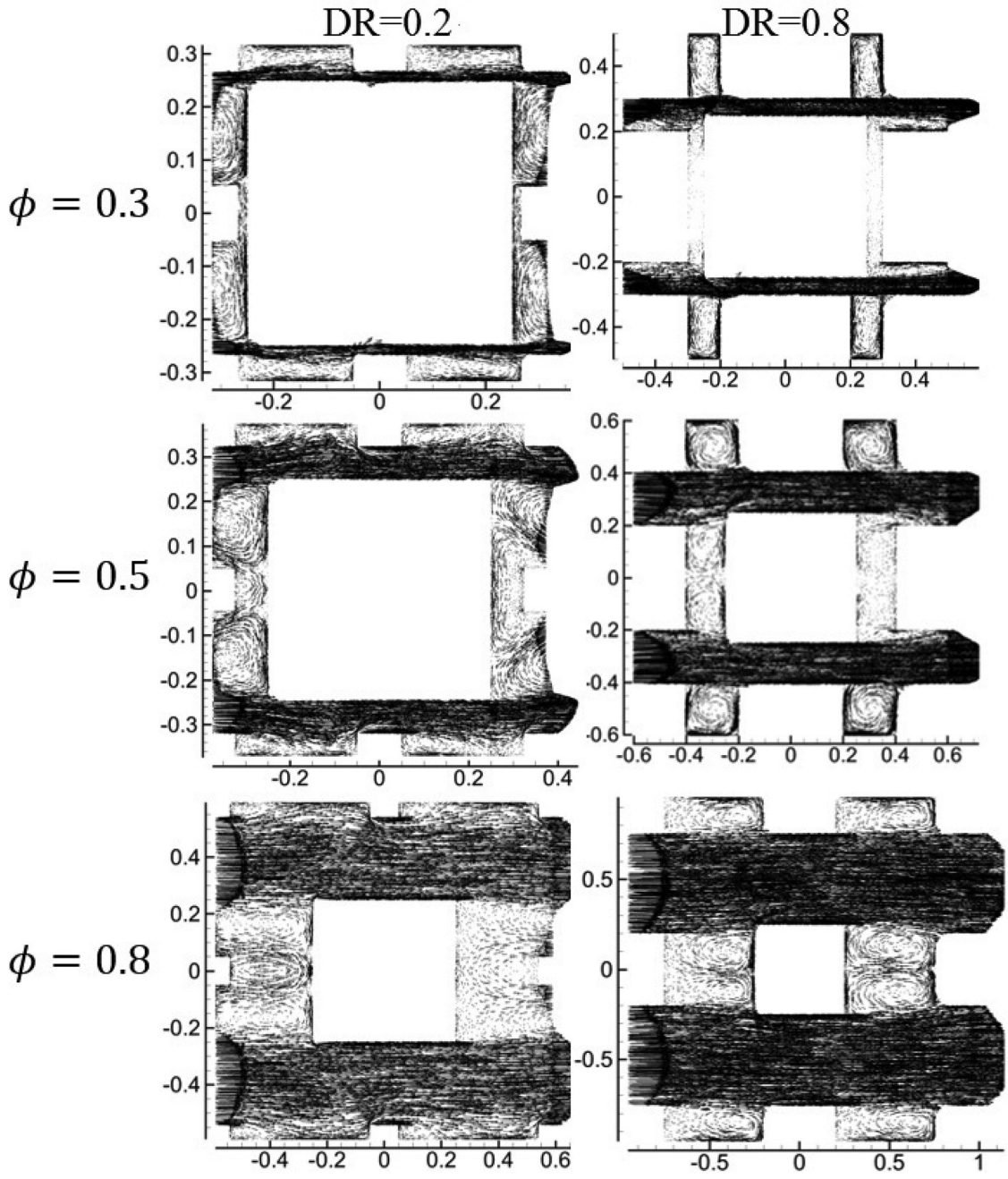

Fig. 17 Velocity vector plots for different domains at $Re_D = 50 \times 10^3$. Axis are *x/H* and *y/H*.

high-vorticity region, which appears near the edges of the square cylinders.

Volume-Averaged Turbulence Parameters, Macroscopic Pressure Gradient, and Friction Factor as a Function of Porosity. Figures 14(*a*)–14(*d*) show the intrinsic volume-averaged k, ε, MPG, and friction factor (f) as functions of ϕ at $Re_D = 50 \times 10^3$. The porosity ϕ ranged from 0.27 to 0.8. This was conveniently realized by modifying the distances H of the original DR domains. In the entire porosity range, the k values for the base case were largest, followed by those of the DR = 0.2 model. The DR = 0.4 and DR = 0.8 models exhibited similar growth tendencies, although with values lower than those of the DR = 0.2 model. At DR = 0.6 and $(1-\phi)/\phi^2 = 3.75$–7.8, the values of k were similar to the values at DR = 0.8.

At $0.3 < (1-\phi)/\phi^2 < 2.0$, the turbulent dissipation rate in the base case was larger than those of the other models. However, at $(1-\phi)/\phi^2 > 3.75$, ε was highest at DR = 0.2. Except for the base case, moderate increases in the turbulent dissipation rate were observed between $(1-\phi)/\phi^2 = 0.3$ and 0.6 for the DR models, suggesting that the flow features did not differ significantly. All the models exhibited linear growth at $(1-\phi)/\phi^2 = 0.6$–7.8.

The behavior of MPG was similar to that of ε. Table 5 lists adjustment constants for k, ε, and MPG, which were obtained using a parabolic function, $f(x) = A + Bx + Cx^2$, with $x = (1-\phi)/\phi^2$. Here, the maximum scatter was estimated to be approximately 3%. This type of function was selected because the conventional power function $f(x) = Ax^n$ did not yield well-correlated values at lower $(1-\phi)/\phi^2$.

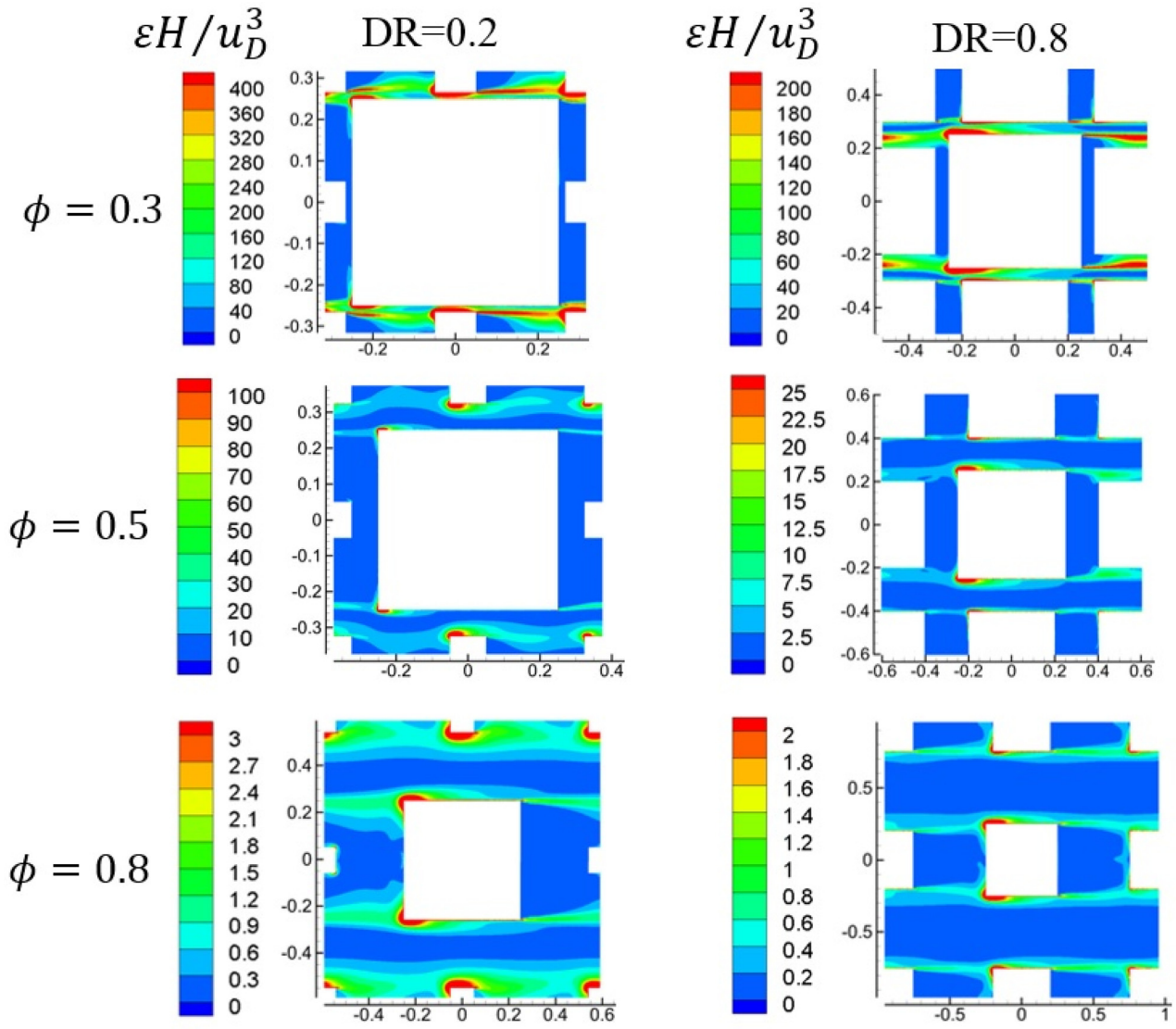

Fig. 18 Contours of dimensionless turbulent kinetic energy dissipation rate at different ϕ and DR obtained at $Re_D = 50 \times 10^3$. Axis in figure are *x/H* and *y/H*.

Figure 14(*d*) shows the friction factor f given by Eq. (14) as a function of $Re_{d_{eq}}$ for the domains with fixed H. In Eq. 14, d_{eq} is estimated from Eq. (15) for square cylinders in a cross flow from Nakayama and Sano [41] and using a corrected diameter, $d_{corr} = (D + d)/2$. For comparison, the base case of DR = 1.0 and the corresponding values from Kundu et al. [21] are also shown. As in the results for k and ε, all the DR models exhibited the same behavior regardless of the value of Re_{eq}. In addition, the values for DR = 0.8 were larger than those of the other models. For a fixed value of H, the highest DR domain had the lowest porosity (ϕ=0.27). As the level of confinement increases, the flow streams have higher velocities, increasing both ε and the pressure losses by friction on the walls.

$$f = -\left(\frac{d\langle p\rangle^f}{dx}\right) \Big/ \left(\frac{\rho_f u_D^2}{2d_{eq}}\right) \tag{14}$$

$$d_{eq} = \sqrt{\frac{32}{120}} \frac{\phi}{1-\phi} d_{corr} \tag{15}$$

Flow Patterns as a Function of ϕ and Diameter Ratio. Figures 15 and 16 show dimensionless contour maps of the mean velocity and vorticity, respectively. The columns refer to the lowest and highest DR values tested, i.e., 0.2 and 0.8, and the rows correspond to different porosity values.

At the highest porosity, $\phi = 0.8$, the flow was characterized by two well-defined high-velocity streams extending along the upper and lower faces of the largest cylinder. Here, the maximum velocities were $u/u_D = 2.5$ and 2.0 for DR = 0.2 and 0.8, respectively. In the gap between the lateral smaller cylinders and the large one, flow gradients with intermediate magnitudes appeared, and the velocity u/u_D ranged between 0.75 and 1.0 for both DR values.

As the porosity decreased to $\phi = 0.5$, the maximum velocities increased by a factor of two, reaching $u/u_D = 5.0$ for DR = 0.2 and $u/u_D = 4.0$ for DR = 0.8. For the lowest porosity, $\phi = 0.3$, the maximum stream velocity was approximately $u/u_D = 10$ for all DR values. For DR = 0.2 and $\phi = 0.5$ and 0.3, the region of maximum velocity coincided with the gap between central small cylinders and the lower and upper face of the large one. For DR = 0.8, the high-velocity regions covered a larger area along the upper and lower faces of the large cylinder.

In all cases, the vorticity was highly concentrated near the corners of all the cylinders. In addition, all the shear layers were elongated in the flow direction and bounded the two main flow streams discussed above. At $\phi = 0.8$, rotational regions appeared

in the spaces in the middle row of cylinders owing to the shear layer and separation of the large cylinder. The vorticity in these regions ranged from $\omega D/u_D = 10$–15 at DR = 0.2 to $\omega D/u_D = 8.0$–12 at DR = 0.8. At the lowest DR, the smaller front- and rear-centered cylinders were fully immersed in the wake of the large cylinder. At DR = 0.8, the wake of the small central cylinder impinged upon the large cylinder, and the rear small cylinder disrupted the wake of the large cylinder, forming another recirculation region. These shear layers are similar to the shielding regime in free flow over four cylinders in an in-line formation [42]. In the gaps between the upper and lower small cylinders at DR = 0.2, the shear layers were extended, forming well-defined lobules, whereas at DR = 0.8, they were disrupted by proximity to the wall. As the porosity decreased further, the proximity to the wall increased, and the shear layers and regions of highest vorticity were closer to each other. For $\phi = 0.3$ and 0.5 and both DR values, the shear layers from the upper and lower small cylinders in front interacted with those of the large cylinder, enhancing the vorticity production. At DR = 0.2 and $\phi = 0.3$, the maximum vorticity was $\omega D/u_D = 500$, which is approximately 20 times that at $\phi = 0.8$. For DR = 0.8, the maximum vorticity increased from 20 at $\phi = 0.8$ to 200 at $\phi = 0.3$. Thus, at the same porosity, the recirculating patterns and their intensities depended on the DR. For the same domains, the corresponding velocity vectors (Fig. 17) show the shapes of the confined vortices. Here, the effective flow areas of the main currents are narrower at lower ϕ because of the presence of the low-velocity recirculation regions. This type of narrowing of the flow channels by eddy formation has also been reported by Chaudhary et al. [43].

Maps of the turbulent dissipation rate are shown in Fig. 18. Like the vorticity, ε was concentrated near the cylinder corners, and it increased even more sharply as the porosity decreased, differing by a factor of more than 100 between the models with the lowest and highest porosities. However, in contrast to the vorticity, the turbulent dissipation rate was low in the spaces between the central cylinder rows (at $y = 0$).

In summary, for all the tested DR values, at higher porosity, the velocity, vorticity, and the turbulent dissipation rate were low, and the shear layers were extended. As the porosity gradually decreased, the velocity of the gap flows increased, the shear layers were disrupted, and vortices were trapped in the low-velocity gaps. The effective flow area was reduced by vortex narrowing. As a consequence of direct interactions between shear layers, the vorticity and the turbulent dissipation rate increased sharply in magnitude, and strong frictional forces were present, as indicated by the high MPG values. On the basis of the volume-averaged profiles in Figs. 14(*a*)–14(*d*), the critical value of ϕ at which the flow parameters increase greatly in magnitude is estimated to be $\phi \approx 0.6$; the largest energetic losses generally appear at DR = 0.2 and the lowest porosity.

Conclusions

The ability of the AKN, LB, YS, STD k–ε, and k–ω LRN turbulence models to predict the volume-averaged quantities was tested using a periodic array of square cylinders. Additionally, the flow patterns inside pores in arrays of square cylinders with different diameter ratios were assessed. The flow was turbulent and covered the Reynolds number range of $Re_D = 500 - 500 \times 10^3$; the porosity ϕ was varied from 0.27 to 0.8, and the DR was varied from 0.2 to 0.8. Overall, all of the LRN turbulence models were able to predict the MPG for all Re_D. However, the values predicted by the YS, LB, and LR k–ω models exhibited discrepancies, especially those of the turbulent kinetic energy, as a function of both ϕ and Re_D. Overall, the AKN model exhibited better agreement.

A diameter ratio analysis yielded the following findings. In all of the scenarios, two main currents transported all of the flow along the domain. At higher porosity ($\phi > 0.6$), the velocities were low, and the streams were wide. Wakes were formed, and the turbulent kinetic energy production, its turbulent dissipation rate, and MPG were typically low. The flow features of the DR models were different from those of an infinite staggered arrangement of square cylinders of the same diameter. Depending on DR, as the porosity decreased, the gap velocities increased, and the shear layers were suppressed by proximity to the wall, forming recirculation zones within the gaps. Consequently, the frictional forces were enhanced, and the turbulence parameters increased greatly. The highest values of the turbulent kinetic energy production and its dissipation rate, as well as the MPG, were observed when the flow confinement was such that the shear layers interacted directly. The highest values were observed for DR = 0.2.

Acknowledgment

The authors are grateful for the insightful comments given by the anonymous peer reviewers. Thanks are also given to Patrick Verdin from Cranfield University for its help to improve the readability of the Manuscript. This research did not receive any specific grant from funding agencies in the public, commercial, or not-for-profit sectors.

Nomenclature

C_μ, $C_{1\varepsilon}$, $C_{2\varepsilon}$, σ_k, σ_ε = constants of the turbulence closure equations
d = small particle diameter (m)
D = large particle diameter (m)
d_{eq} = equivalent diameter (m)
d_{corr} = corrected diameter (m)
f = friction factor
f_1, f_2, f_μ = damping functions of the LRN turbulence models
H = representative volume element height/lenght (m)
k = turbulent kinetic energy (m^2/s^2)
$\langle k \rangle^f$ = intrinsic volume average turbulent kinetic energy (m^2/s^2)
P = pressure (N/m^2)
$\langle P \rangle^f$ = fluid volume average pressure (N/m^2)
Re_D = Reynolds number based on largest particle diameter and Darcy velocity ($u_D D/\nu$)
Re_{eq} = equivalent Reynolds number
Re_p = pore Reynolds number ($\langle u \rangle^f D/\nu$)
R_t = turbulence Reynolds number for damping function ($k^2/\nu\varepsilon$)
$R_{t\omega}$ = turbulence Reynolds number for damping function ($k/\nu\omega$)
R_y = turbulence Reynolds number for damping function ($y\sqrt{k}/\nu$)
u_D = Darcian velocity (m/s)
u_K = Kolmogorov velocity scale (m/s)
u_τ = friction velocity ($\sqrt{\tau_w/\rho}$) (m/s)
$\overline{u}_i$ = time-averaged velocity vector (m/s)
$\langle u \rangle^f$ = intrinsic volume average velocity (m/s)
V = total volume (m^3)
V_f = fluid volume (m^3)
x_i = Cartesian coordinates (m)
y^+ = dimensionless wall distance ($u_\tau y/\nu$)
y^* = dimensionless wall distance ($y^* = u_K y/\nu$)
α^*_∞, α^*_0, = $k - \omega$ model constants
ε = turbulent kinetic energy dissipation rate (m^2/s^3)
$\langle \varepsilon \rangle^f$ = intrinsic volume average turbulent kinetic energy dissipation rate (m^2/s^3)
μ = molecular viscosity (Pa·s)
μ_t = turbulent viscosity (Pa·s)
ϕ = porosity
ω = dissipation per unit turbulent kinetic energy ($\rho k/\mu_t$), vorticity magnitude (1/s)

$\langle\omega\rangle^f$ = intrinsic volume average vorticity magnitude (1/s)
ρ_f = fluid density (kg/m^3)
$\rho\overline{u_i' u_j'}$ = Reynolds stresses (Pa)
τ_w = wall shear stress (N/m^2)
ν = kinematic viscosity (m^2/s)
ν_t = kinematic turbulent viscosity (m^2/s)

References

[1] Dybss, A., and Edwards, R., 1984, "A New Look at Porous Media Fluid mechanics -Darcy to Turbulent," *Fundamentals of Transport Phenomena in Porous Media, Proceedings of the NATO Advanced Study Institute on Mechanics of Fluids in Porous Media*, 1 ed., J. Bear and Y. Corapcioglu, eds., Martinus Nijhoff Publishers, Newark, DE, pp. 199–256.

[2] Weitzman, J. S., Samuel, L. C., Craig, A. E., Zeller, R. B., Monismith, S. G., and Koseff, J. R., 2014, "On the Use of Refractive - Index – Matched Hydrogel for Fluid Velocity Measurement Within and Around Geometrically Complex Solid Obstructions," Exp. Fluids, **55**(12), pp. 1–12.

[3] Wood, B. D., He, X., and Apte, S. V., 2020, "Modeling Turbulent Flows in Porous Media," Annu. Rev. Fluid Mech., **52**(1), pp. 171–203.

[4] Jiang, X., and Lai, H., 2009, *Numerical Techniques for Direct and Large-Eddy Simulations*, 1st ed., CRC Press, Boca Raton, FL.

[5] Jin, Y., Uth, M. F., Kuznetsov, A. V., and Herwig, H., 2015, "Numerical Investigation of the Possibility of Macroscopic Turbulence in Porous Media: A Direct Numerical Simulation Study," J. Fluid Mech., **766**, pp. 76–103.

[6] Chu, X., Weigand, B., and Vaikuntanathan, V., 2018, "Flow Turbulence Topology in Regular Porous Media: From Macroscopic to Microscopic Scale With Direct Numerical Simulation," Phys. Fluids, **30**(6), p. 065102.

[7] Rasam, A., Brethouwer, G., Schlatter, P., Li, Q., and Johansson, A. V., 2011, "Effects of Modelling, Resolution and Anisotropy of Subgrid-Scales on Large Eddy Simulations of Channel Flow," J. Turbul., **12**, pp. N10–N19.

[8] Kuwata, Y., and Suga, K., 2015, "Large Eddy Simulations of Pore-Scale Turbulent Flows in Porous Media by the Lattice Boltzmann Method," Int. J. Heat Fluid Flow, **55**, pp. 143–157.

[9] Suga, K., Chikasue, R., and Kuwata, Y., 2017, "Modelling Turbulent and Dispersion Heat Fluxes in Turbulent Porous Medium Flows Using the Resolved LES Data," Int. J. Heat Fluid Flow, **68**, pp. 225–236.

[10] Hrenya, C., Bolio, E., Chakrabarti, D., and Sinclair, J., 1995, "Comparison of Low Reynolds Number k-ϵ Turbulence Models in Predicting Fully Developed Pipe Flow," Int. J. Heat Mass Transfer, **50**(12), pp. 1923–1941.

[11] Kuwahara, F., Yamane, T., and Nakayama, A., 2006, "Large Eddy Simulation of Turbulent Flow in Porous Media," Int. Commun. Heat Mass Transfer, **33**(4), pp. 411–418.

[12] Kundu, P., Kumar, V., Hoarau, Y., and Mishra, I. M., 2016, "Numerical Simulation and Analysis of Fluid Flow Hydrodynamics Through a Structured Array of Circular Cylinders Forming Porous Medium," Appl. Math. Modell., **40**(23–24), pp. 9848–9871.

[13] Tu, J., Yeoh, G.-H., and Liu, C., 2009, *Computational Fluid Dynamics, a Practical Approach*, 2nd ed., Butterworth-Heinemann, Woburn, MA.

[14] Wilcox, D. C., 1993, *Turbulence Modeling for CFD*, 3rd ed., DCW Industries, La Canada, CA.

[15] Antohe, B., and Lage, J., 1997, "A General Two-Equation Macroscopic Turbulence Model for Incompressible Flow in Porous Media," Int. J. Heat Mass Transfer, **40**(13), pp. 3013–3024.

[16] Yang, J., Zhou, M., Li, S. Y., Bu, S. S., and Wang, Q. W., 2014, "Three-Dimensional Numerical Analysis of Turbulent Flow in Porous Media Formed by Periodic Arrays of Cubic, Spherical, or Ellipsoidal Particles," ASME J. Fluids Eng., **136**(1), pp. 15–24.

[17] Masuoka, T., and Takatsu, Y., 1996, "Turbulence Model for Flow Through Porous Media," Int. J. Heat Mass Transfer, **39**(13), pp. 2803–2809.

[18] Nakayama, A., and Kuwahara, F., 1999, "A Macroscopic Turbulence Model for Flow in a Porous Medium," ASME J. Fluids Eng., **121**(2), pp. 427–433.

[19] Nakayama, A., and Kuwahara, F., 2008, "A General Macroscopic Turbulence Model for Flows in Packed Beds, Channels, Pipes, and Rod Bundles," ASME J. Fluids Eng., **130**(10), p. 101205.

[20] Pedras, M., and de Lemos, M. J., 2001, "Macroscopic Turbulence Modeling for Incompressible Flow Through Undeformable Porous Media," Int. J. Heat Mass Transfer, **44**(6), pp. 1081–1093.

[21] Kundu, P., Kumar, V., and Mishra, I. M., 2014, "Numerical Modeling of Turbulent Flow Through Isotropic Porous Media," Int. J. Heat Mass Transfer, **75**, pp. 40–57.

[22] Hassid, S., and Poreh, M., 1975, "A Turbulent Energy Model for Flows With Drag Reduction," ASME J. Fluids Eng., **97**(2), pp. 234–241.

[23] Lam, C. K. G., and Bremhorst, K., 1981, "A Modified Form of the k-Epsilon Model for Predicting Wall Turbulence," ASME J. Fluids Eng., **103**(3), pp. 456–460.

[24] Abe, K., Kondoh, T., and Nagano, Y., 1994, "A New Turbulence Model for Predicting Fluid Flow and Heat Transfer in Separating and Reattaching flows-I. Flow Field Calculations," Int. J. Heat Mass Transfer, **37**(1), pp. 139–151.

[25] Yang, Z., and Shih, Y., 1993, "New Time Scale Based k-Epsilon Model for Near-Wall Turbulence," AIAA J., **31**(7), pp. 1191–1198.

[26] Kuwahara, F., Kameyama, Y., Yamashita, S., and Nakayama, A., 1998, "Numerical Modeling of Turbulent Flow in Porous Media Using a Spatially Periodic Array," J. Porous Media, **1**(1), pp. 47–55.

[27] Abudu, P., Wang, L., Xu, M., Jia, D., Wang, X., and Jia, L., 2018, "Hierarchical Porous Carbon Materials Derived From Petroleum Pitch for High-Performance Supercapacitors," Chem. Phys. Lett., **702**, pp. 1–7.

[28] Roucher, A., Schmitt, V., Blin, J. L., and Backov, R., 2019, "Sol–Gel Process and Complex Fluids: Sculpting Porous Matter at Various Lengths Scales Towards the Si(HIPE), Si(PHIPE), and SBA-15-Si(HIPE) Series," J. Sol–Gel Sci. Technol., **90**(1), pp. 95–104.

[29] Joshi, R., Schneider, J. J., Yilmazoglu, O., and Pavlidis, D., 2010, "Patterned Growth of Ultra Long Carbon Nanotubes. Properties and Systematic Investigation Into Their Growth Process," J. Mater. Chem., **20**(9), pp. 1717–1721.

[30] Zuluaga, L. F., Fossen, H., Ballas, G., and Rotevatn, A., 2018, "Structural and Petrophysical Effects of Overthrusting on Highly Porous Sandstones: The Aztec Sandstone in the Buffington Window, SE Nevada, USA," Geol. Soc., London, Spec. Publ., **459**(1), pp. 59–77.

[31] Abe, K., Nagano, Y., and Kondoh, T., 1993, "Numerical Prediction of Separating and Reattaching Flows With a Modified low-Reynolds-Number k-ϵ Model," J. Wind Eng. Ind. Aerodyn., **46–47**, pp. 85–94.

[32] Guo, B., Yu, A., Wright, B., and Zulli, P., 2006, "Simulation of Turbulent Flow in a Packed Bed," Chem. Eng. Technol., **29**(5), pp. 596–603.

[33] ANSYS, 2016, *Meshing 17.0*., ANSYS, Canonsburg, PA.

[34] Celik, I., and Karatekin, O., 1997, "Numerical Experiments on Application of Richardson Extrapolation With Nonuniform Grids," ASME J. Fluids Eng., **119**(3), pp. 584–590.

[35] Coroneo, M., Montante, G., Paglianti, A., and Magelli, F., 2011, "CFD Prediction of Fluid Flow and Mixing in Stirred Tanks: Numerical Issues About the RANS Simulations," Comput. Chem. Eng., **35**(10), pp. 1959–1968.

[36] Teruel, F. E., and Rizwan-Uddin, 2010, "Numerical Computation of Macroscopic Turbulence Quantities in Representative Elementary Volumes of the Porous Medium," Int. J. Heat Mass Transfer, **53**(23–24), pp. 5190–5198.

[37] de Lemos, M. J. S., 2012, *Turbulence in Porous Media: Modeling and Applications*, 2nd ed., Elsevier, London.

[38] Larsson, I. A., Lundström, T. S., and Lycksam, H., 2018, "Tomographic PIV of Flow Through Ordered Thin Porous Media," Exp. Fluids, **59**(6), pp. 1–7.

[39] Agnaou, M., Lasseux, D., and Ahmadi, A., 2016, "From Steady to Unsteady Laminar Flow in Model Porous Structures: An Investigation of the First Hopf Bifurcation," Comput. Fluids, **136**, pp. 67–82.

[40] Delafosse, A., Morchain, J., Guiraud, P., and Liné, A., 2009, "Trailing Vortices Generated by a Rushton Turbine: Assessment of URANS and Large Eddy Simulations," Chem. Eng. Res. Des., **87**(4), pp. 401–411.

[41] Nakayama, A., Kuwahara, F., and Sano, Y., 2007, "Concept of Equivalent Diameter for Heat and Fluid Flow in Porous Media," AIChE J., **53**(3), pp. 732–736.

[42] Lam, K., and Zou, L., 2010, "Three-Dimensional Numerical Simulations of Cross-Flow Around Four Cylinders in an in-Line Square Configuration," J. Fluids Struct., **26**(3), pp. 482–502.

[43] Chaudhary, K., Cardenas, M. B., Deng, W., and Bennett, P. C., 2011, "The Role of Eddies Inside Pores in the Transition From Darcy to Forchheimer Flows," Geophys. Res. Lett., **38**(24), p. 6.